FINITE ELEMENT MODELING OF WAVE PROPAGATION IN CONCRETE

FINAL REPORT

SPR 633

FINITE ELEMENT MODELING OF WAVE PROPAGATION IN CONCRETE

Final Report

SPR 633

by

T. C. Kennedy, S. C. Lovejoy, and J. E. Blomberg
Oregon State University
Oregon Department of Transportation

for

Oregon Department of Transportation
Research Unit
200 Hawthorne Ave. SE, Suite B-240
Salem OR 97301-5192

and

Federal Highway Administration
400 Seventh Street, SW
Washington, DC 20590-0003

September 2008

Technical Report Documentation Page

1. Report No. FHWA-OR-RD-09-06	2. Government Accession No.	3. Recipient's Catalog No.

4. Title and Subtitle Finite Element Modeling of Wave Propagation in Concrete	5. Report Date September 2008 6. Performing Organization Code
7. Author(s) T. C. Kennedy, S. C. Lovejoy, and J. E. Blomberg	8. Performing Organization Report No.
9. Performing Organization Name and Address Oregon State University 220 Owen Hall Corvallis, OR 97331-3212	10. Work Unit No. (TRAIS) 11. Contract or Grant No. SPR 633
12. Sponsoring Agency Name and Address Oregon Department of Transportation Research Unit and Federal Highway Administration 200 Hawthorne Ave. SE, Suite B-240 Salem, OR 97301-5192 Federal Highway Administration 400 Seventh Street, SW Washington, DC 20590-0003	13. Type of Report and Period Covered Final Report 14. Sponsoring Agency Code

15. Supplementary Notes

16. Abstract

Three reports were produced from research sponsored by the Oregon Department of Transportation on acoustic emission (AE). The first describes the evaluation of AE techniques applied to two reinforced concrete (RC) bridge girders, which were loaded to mimic in-service conditions. The main goal was to get a thorough understanding of how AE methods can be used with RC and in what way these methods can assist in maintaining the state's aging RC deck girder bridges. Recommended settings for data acquisition and processing were evaluated. In addition to the complex full-scale beam components, studies were performed on smaller test specimens that improved understanding of stress wave propagation through reinforced concrete and the response of acoustic emission sensors in detecting these waves. Some qualitative and quantitative assessment methodologies were described, and examples and limitations of the methods were presented. Source locations in three dimensions were performed, and strategies on how to best deploy sensors were evaluated using Monte Carlo Simulations.

17. Key Words Stress wave, bridge design, deconvolution, finite elements	18. Distribution Statement Copies available from NTIS, and online at http://www.oregon.gov/ODOT/TD/TP_RES/

19. Security Classification (of this report) Unclassified	20. Security Classification (of this page) Unclassified	21. No. of Pages 80	22. Price

Technical Report Form DOT F 1700.7 (8-72) Reproduction of completed page authorized Printed on recycled paper

SI* (MODERN METRIC) CONVERSION FACTORS

APPROXIMATE CONVERSIONS TO SI UNITS

Symbol	When You Know	Multiply By	To Find	Symbol
		LENGTH		
in	inches	25.4	millimeters	mm
ft	feet	0.305	meters	m
yd	yards	0.914	meters	m
mi	miles	1.61	kilometers	km
		AREA		
in^2	square inches	645.2	millimeters squared	mm^2
ft^2	square feet	0.093	meters squared	m^2
yd^2	square yards	0.836	meters squared	m^2
ac	acres	0.405	hectares	ha
mi^2	square miles	2.59	kilometers squared	km^2
		VOLUME		
fl oz	fluid ounces	29.57	milliliters	ml
gal	gallons	3.785	liters	L
ft^3	cubic feet	0.028	meters cubed	m^3
yd^3	cubic yards	0.765	meters cubed	m^3
	NOTE: Volumes greater than 1000 L shall be shown in m^3.			
		MASS		
oz	ounces	28.35	grams	g
lb	pounds	0.454	kilograms	kg
T	short tons (2000 lb)	0.907	megagrams	Mg
		TEMPERATURE (exact)		
°F	Fahrenheit	(F-32)/1.8	Celsius	°C

APPROXIMATE CONVERSIONS FROM SI UNITS

Symbol	When You Know	Multiply By	To Find	Symbol
		LENGTH		
mm	millimeters	0.039	inches	in
m	meters	3.28	feet	ft
m	meters	1.09	yards	yd
km	kilometers	0.621	miles	mi
		AREA		
mm^2	millimeters squared	0.0016	square inches	in^2
m^2	meters squared	10.764	square feet	ft^2
m^2	meters squared	1.196	square yards	yd^2
ha	hectares	2.47	acres	ac
km^2	kilometers squared	0.386	square miles	mi^2
		VOLUME		
ml	milliliters	0.034	fluid ounces	fl oz
L	liters	0.264	gallons	gal
m^3	meters cubed	35.315	cubic feet	ft^3
m^3	meters cubed	1.308	cubic yards	yd^3
		MASS		
g	grams	0.035	ounces	oz
kg	kilograms	2.205	pounds	lb
Mg	megagrams	1.102	short tons (2000 lb)	T
		TEMPERATURE (exact)		
°C	Celsius	1.8C+32	Fahrenheit	°F

*SI is the symbol for the International System of Measurement

ACKNOWLEDGEMENTS

The Authors are indebted to Mr. Gary Barquist for fabricating the large number of test specimens used in this project.

DISCLAIMER

TABLE OF CONTENTS

APPENDICIES

TABLE OF TABLES

TABLE OF FIGURES

1.0 INTRODUCTION

The Oregon Department of Transportation has a need to develop accurate methods for assessing the remaining service life of vintage bridges throughout the state of Oregon. As these bridges continue to age and accumulate damage, their current condition and in-service performance will need to be monitored; one method under consideration for accomplishing this is through acoustic emission (AE) testing. This approach is based on the principle that structural damage releases energy, some of which is manifested through stress wave propagation. Sensors, typically mounted on the surface of a structure, can detect these disturbances and produce an electrical output that is a function of the disturbance at the site of the sensor. The primary advantage of AE testing when compared to other forms of nondestructive evaluation is that it is very sensitive to the creation of damage as it happens, whereas other methods such as radiography and ultrasonic testing are only sensitive to the accumulation of damage; and thus, in cyclic loading situations, many cycles of damage may need to be imparted before detection can be made. Recent research by Lovejoy (*2006*) took the current state of the art of practical application of AE testing on concrete structures and developed specific testing, data analysis, and interpretation recommendations as they apply to vintage reinforced concrete deck girder bridges subject to diagonal tension cracking. To further support this research effort, there is a need to have modeling capabilities that can be used to interpret acoustic emission data. The objective of the current research project is to evaluate the capability of finite element analysis to accurately simulate the propagation of waves through reinforced concrete. This objective was accomplished by performing some very basic stress wave propagation tests on both not reinforced and reinforced concrete specimens and by comparing the test results to computer predictions. The results of this work are described below.

2.0 CONCRETE PROPERTIES

The material properties of concrete needed for the finite element analysis were determined through some very basic wave propagation tests. The surface response of a homogeneous elastic half-space due to a point impact consists of three parts, the dilatational or pressure wave, the transverse or shear wave, and the Rayleigh wave. The dilatational wave speed, c_d, and shear wave speed, c_s, in a homogeneous elastic isotropic half-space material with elastic modulus E, density ρ, and Poisson's ratio ν, can be calculated using

$$c_d = \sqrt{\frac{E\left(1-\nu\right)}{\rho\left(1+\nu\right)\left(1-2\,\nu\right)}} \tag{2-1}$$

$$c_s = \sqrt{\frac{E}{2\left(1+\nu\right)\rho}} \tag{2-2}$$

Using the dilatational and shear wave speeds, the Rayleigh wave speed can be calculated from

$$\left(2-\frac{c_R^2}{c_s^2}\right)^2 = 4\left(1-\frac{c_R^2}{c_d^2}\right)^{1/2}\left(1-\frac{c_R^2}{c_s^2}\right)^{1/2} \tag{2-3}$$

The relative amplitudes of the dilatational and shear waves become small compared to the Rayleigh wave with increasing distance from the wave source; and for all known materials, the dilatational wave is the fastest. Knowing this, the arrival of the dilatational and Rayleigh waves can be experimentally observed from surface displacement history plots. The dilatational wave speed was experimentally measured by Lovejoy (*2006*) by sending a pulse through a cylindrical concrete specimen to a sensor on the opposite end and recording the time the wave needed to travel the length of the cylinder (Figure 2.1). The dilatational wave velocity can be calculated by dividing the length of the test specimen by the time required for the wave to reach the other end. The test specimen was poured from the same concrete mix as the larger test specimens described in:

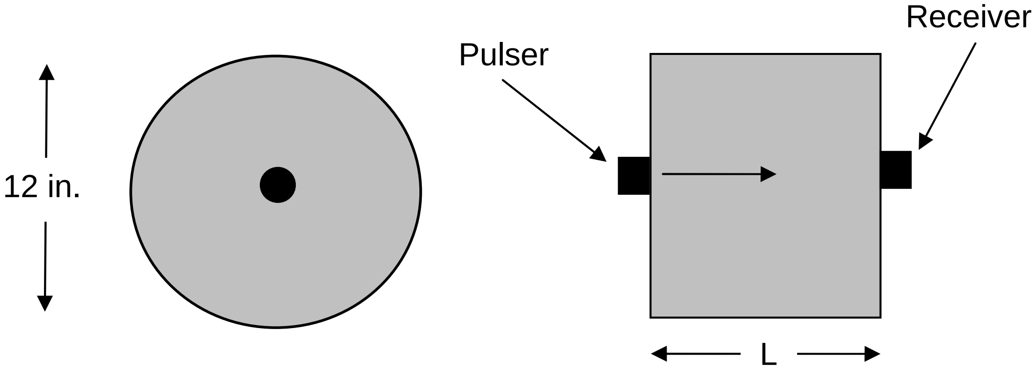

Figure 2.1: Dilatational wave measurement set up

A dilatational wave speed of 150 in/ms was measured and this value was used for all subsequent simulations.

The density of the material was obtained by dividing the weight of the cylindrical test specimen by the measured volume to produce a value of 141lbm/ft^3.

The Rayleigh wave speed was determined using a cross-correlation method on the surface displacement time histories of two sensors. The first sensor, S_1, is located a distance, r, away for the wave source and a second senor, S_2, is placed a distance; d, away from S_1 (Figure 2.2). The distance r must be large enough such that the Rayleigh wave carries most of the energy (*Sinha 1983*).

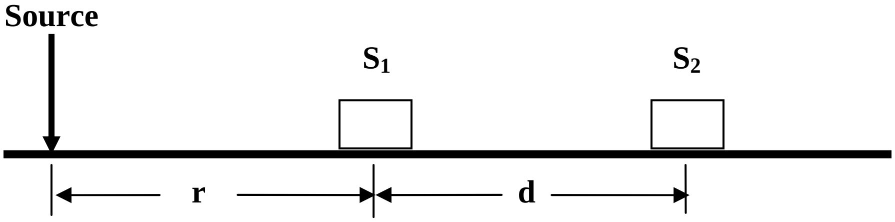

Figure 2.2: Sensor locations for determining the Rayleigh wave speed

Let $h_1(t)$, $h_2(t)$ represent the surface displacement time histories for sensors S_1, S_2 respectively. The cross-correlation function is defined as

$$z(t) = \int_{-\infty}^{\infty} h_1(\tau)\, h_2(t+\tau)\, d\tau \qquad \textbf{(2-4)}$$

If the signals $h_1(t)$ and $h_2(t)$ are similar in shape and differ by a time delay, Δt, then the maximum of the cross-correlation function occurs when t = Δt. Since the arrival of the Rayleigh wave will cause similar surface displacements at both sensor locations, the cross-correlation function will compute the time, Δt, required for the Rayleigh wave to travel the distance d. The velocity of the Rayleigh wave can be calculated by dividing the distance d by time Δt [2]. Due to the complex loading curve and the sensor properties, the time history data was reduced to only include the first relatively large displacement oscillations. This reduced the effect of low amplitude vibration and signal noise of the receiver for determining the Rayleigh wave speed.

Figure 2.3 shows the calculated Rayleigh wave speeds for varying d and r distances. Notice that for small sensor separation distances d and for small values of r, faster Rayleigh wave speeds were calculated. At greater distances from the source and when the sensors were again close together, the calculated Rayleigh wave speeds were slower. The calculated Rayleigh wave speeds tend to converge when d is greater than nine inches. An average Rayleigh wave speed of 78.6 in/ms was calculated for d greater than nine inches. The variation in the calculated wave speed is believed to be caused by the aggregate in the concrete. When the two receiving sensors are far apart, the effect of the aggregate on the wave speed is averaged out, and a global wave speed is measured; when the sensors are relatively close together, the presence of aggregate results in a localized wave speed measurement.

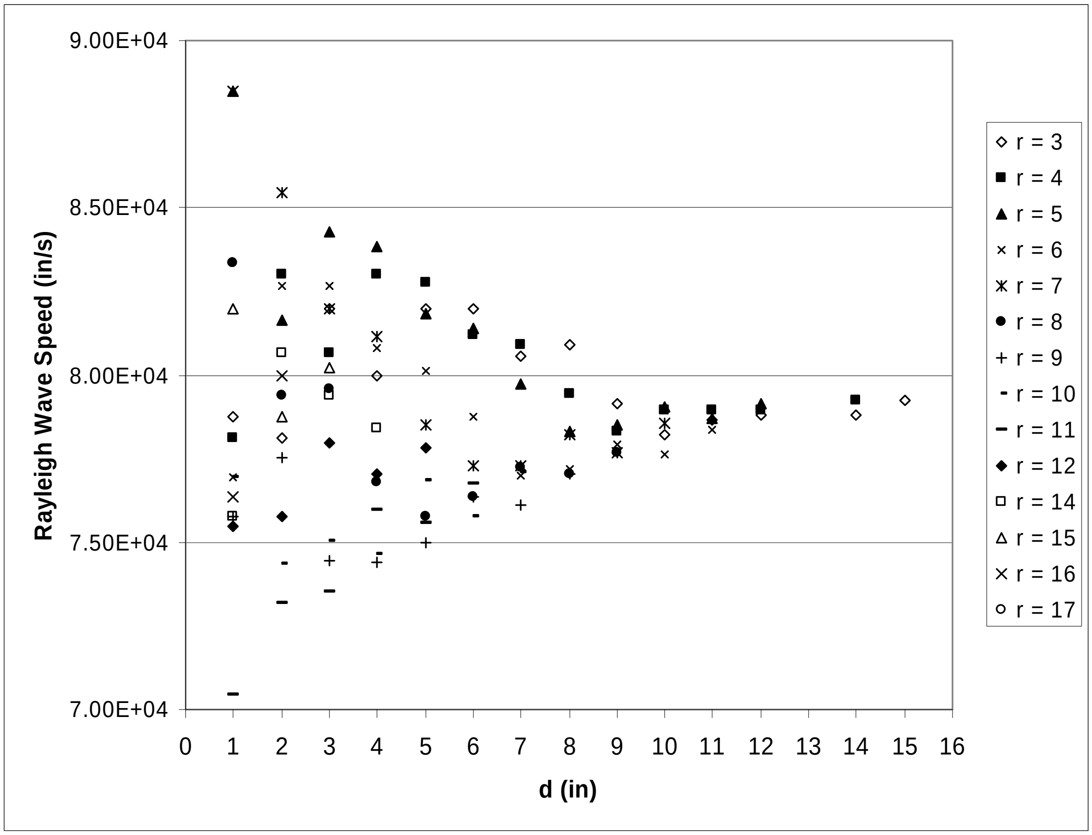

Figure 2.3: Calculated Rayleigh speeds for varying r and d distances

The shear wave speed, c_s, can be calculated from the experimentally measured c_d and c_R wave speeds using eq (2-3). With the experimentally measured density, dilatational and Rayleigh wave speeds, the material properties could be calculated using

$$E = 2\left(c_s^2\,\rho + c_s^2\,\nu\,\rho\right) \tag{2-5}$$

$$\nu = \frac{c_d^2 - 2\,c_s^2}{2\left(c_d^2 - c_s^2\right)} \tag{2-6}$$

The properties are summarized in Table 2.1

Table 2.1: Measured Material Properties

Dilatational wave speed	$c_d = 150x10^3 \ \ {}^{in}\!/_{s}$
Rayleigh wave speed	$c_R = 78.6 \ \ {}^{in}\!/_{s}$
Shear wave speed	$c_s = 83.1 \ \ {}^{in}\!/_{s}$
Density	$\rho = 2.112x10^{-4} \ \ {}^{lb\,s^2}\!/_{in^4}$
Elastic modulus	$E = 3.73x10^6 \ \ {}^{lb}\!/_{in^2}$
Poisson's ratio	$\upsilon = 0.28$

Attenuation or damping of an acoustic waveform in a material is a function of three processes; spreading, scattering, and absorption (*Landis 1995*). Spreading is a geometric function causing the wave amplitude to decrease as it spreads out over a larger area while scattering and absorption are dependent on material properties. Scattering of the wave as it impinges upon particles of aggregate is the most likely mechanism for the attenuation in concrete. The geometric attenuation of the waveforms was automatically accounted for in the model, and global mass damping was added to account for the scattering and absorption. It was assumed that there was no frequency dependent damping that can affect ultrasonic properties such as pulse velocity. Losses associated with the coupling of the sensor to the test specimen were considered to be included in the mass damping coefficient. The mass damping factor, D, was varied to simulate losses in the material and test setup and appropriate values were chosen to be typical of concrete i.e.

$$2\% \le \frac{D}{2\,\omega} \le 4\% \tag{2-7}$$

Where ω is the frequency of the excitation source.

3.0 SIGNAL ANALYSIS AND FINITE ELEMENT MODEL VERIFICATION

This section describes theoretical analyses performed for purposes of experimental data interpretation and finite element model verification.

3.1 FORCING FUNCTION ANALYSIS

A practical method for imparting an acoustic emission source into a structure is through the use of a pulse sensor. An AE sensor with pulse-through capability is mounted on the structure. An oscillatory voltage is sent to the sensor causing the sensor to excite the structure. Although the input voltage to the sensor is known, the actual forcing function applied to the surface of the structure must be determined in an indirect manner. A common technique (*Knopoff 1958*) for accomplishing this is to mount an exciter senor and a receiver sensor on opposite sides of a homogeneous, elastic material (e.g., aluminum) a deconvolution process is applied to the received signal in order to determine the forcing function. This process is described below.

We begin with the case of an infinite plate of thickness b subjected to a point source of stress directed normal to one face and a unit step function in time. The normal component of displacement on the opposite face was determined by Knopoff (*1958*) as

$$u_h = \frac{1}{\pi G b}\left[\begin{array}{l} \dfrac{w^2(2w^2-2+a^{-2})^2a^{-2}}{[(2w^2-2+a^{-2})^2-4w(w^2-1)(w^2-1+a^{-2})^{1/2}]^2}H(t-b/c_d) \\ -\dfrac{4y^2(y^2-1)(y^2+a^2-1)}{[(2y^2-1)^2-4y(y^2-1)(y^2+a^2-1)^{1/2}]^2}H(t-b/c_s) \end{array}\right] \qquad \textbf{(3-1)}$$

Where

$$w=c_dt/b \qquad \textbf{(3-2)}$$

$$y=c_st/b \qquad \textbf{(3-3)}$$

$$a=c_s/c_d \qquad \textbf{(3-4)}$$

G is the shear modulus, and H is the Heaviside step function. Equation (3-1) is valid up to the second reflection of the dilatational wave. If the excitation is some arbitrary function of time f(t) rather than a step function, the normal component of displacement v(t) on the opposite face becomes (*Graff 1975*)

$$v(t)=\int_0^t f'(\xi)u_h(t-\xi)d\xi \qquad \textbf{(3-5)}$$

Where f'(t) is the derivative of f(t). In our experiment we measure v(t) and want to use this to determine f(t). We can accomplish this through a deconvolution process. First, we make the change of variable ζ=t-ξ in eq. (3-2) to obtain

$$v(t) = \int_0^t f'(t-\varsigma)u_h(\varsigma)d\varsigma \qquad \textbf{(3-6)}$$

Due to the nature of $u_h(\zeta)$, we can rewrite eq. (3-6) as

$$v(t) = \int_{b/c_d}^t f'(t-\varsigma)u_h(\varsigma)d\varsigma \qquad \textbf{(3-7)}$$

To evaluate the integral we treat this as a problem of trying to approximate the area under a curve by summing up the areas of a number of rectangular regions as shown in Figure 3.1.

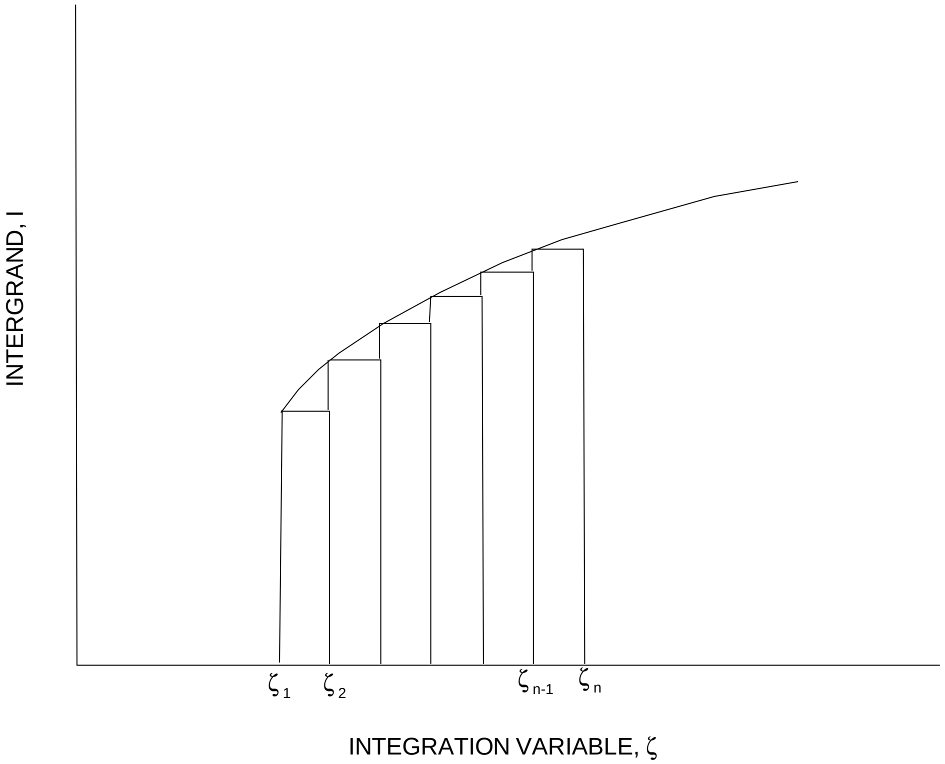

Figure 3.1: Approximation of the integral by a summation of rectangular areas

Thus, we obtain

$$v(t) = \sum_{j=1}^{n-1} f'(t - \varsigma_j) u_h(\varsigma_j) \Delta\varsigma \qquad \textbf{(3-8)}$$

Where $\Delta\zeta$ is the width of each rectangle. We will evaluate v(t) at n discrete points in time where

$$t=b/c_d+i\Delta t \qquad i=1,2,\ldots n \qquad \textbf{(3-9)}$$

We let

$$\Delta\zeta=\Delta t \qquad \textbf{(3-10)}$$

$$\zeta_j=b/c_d+(j-1)\Delta t \qquad \textbf{(3-11)}$$

This gives

$$v(b/c_d + i\Delta t) = \sum_{j=1}^{i} f'[i\Delta t - (j-1)\Delta t] u_h[b/c_d + (j-1)\Delta t]\Delta t \qquad i=1,2,\ldots n \qquad \textbf{(3-12)}$$

After some manipulations [7] we arrive at a recursive relation for f'(t) as

$$f'(i\Delta t) = \frac{1}{u_h(b/c_d)}\left[v(b/c_d + i\Delta t)/\Delta t - \sum_{j=1}^{i-1} f'[(i-j)\Delta t] u_h[b/c_d + j\Delta t] \right] \quad i=1,2,\ldots n \qquad \textbf{(3-13)}$$

With f'(t) determined, f (t) can be found by numerical integration.

An experiment was performed on a 9.5inx9.5inx4in block of aluminum as shown in Figure 3.2. A Vallen DECI S1000H hi-fidelity sensor was mounted at the center on one side of the block and served as the source excitation. A Glaser-NIST conical transducer was mounted on the opposite side and served as a receiver. This AE receiver was chosen because it was found to mostly closely respond to surface displacements when compared to the more common resonant type AE transducers (*Schumacher 2008*). The input voltage (normal calibration pulse) to the excitation sensor is shown in Figure 3.3. The signal received by the sensor on the opposite face is shown in Figure 3.4. A calibration for the receiver sensor to convert voltage to displacement was not available. Therefore, a factor of 10^{-8}in/mV was used to produce physically reasonable values of force and displacement. The deconvolution process was applied to the received signal, and the resulting forcing function is shown in Figure 3.5.

Figure 3.2: Calibration test on an aluminum block.

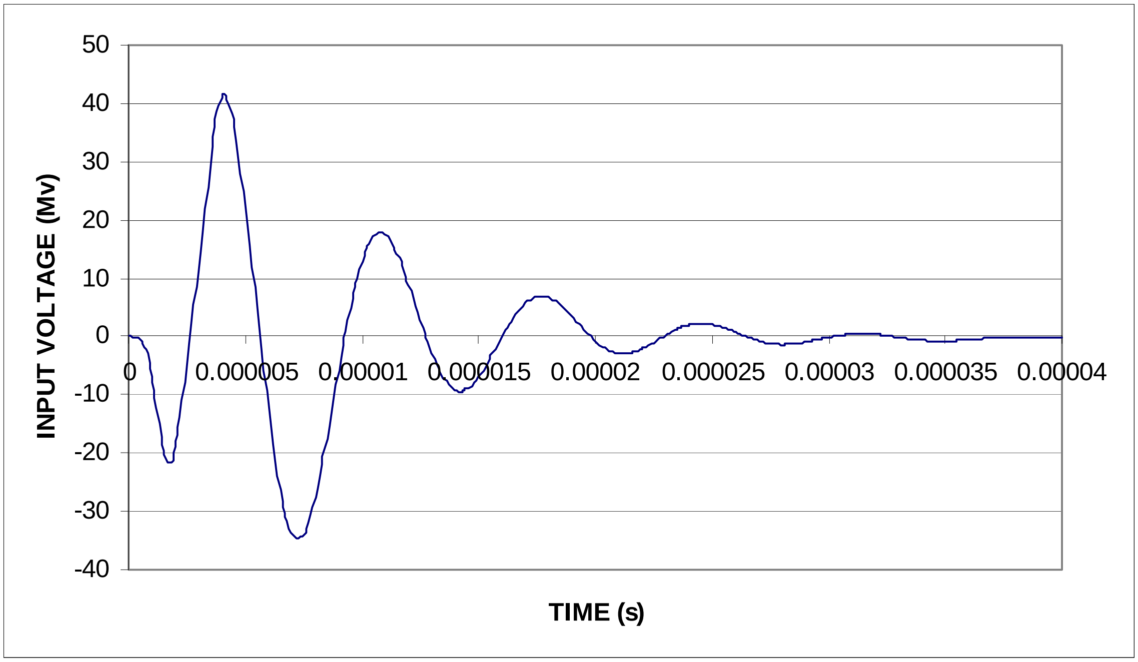

Figure 3.3: Input voltage to excitation sensor

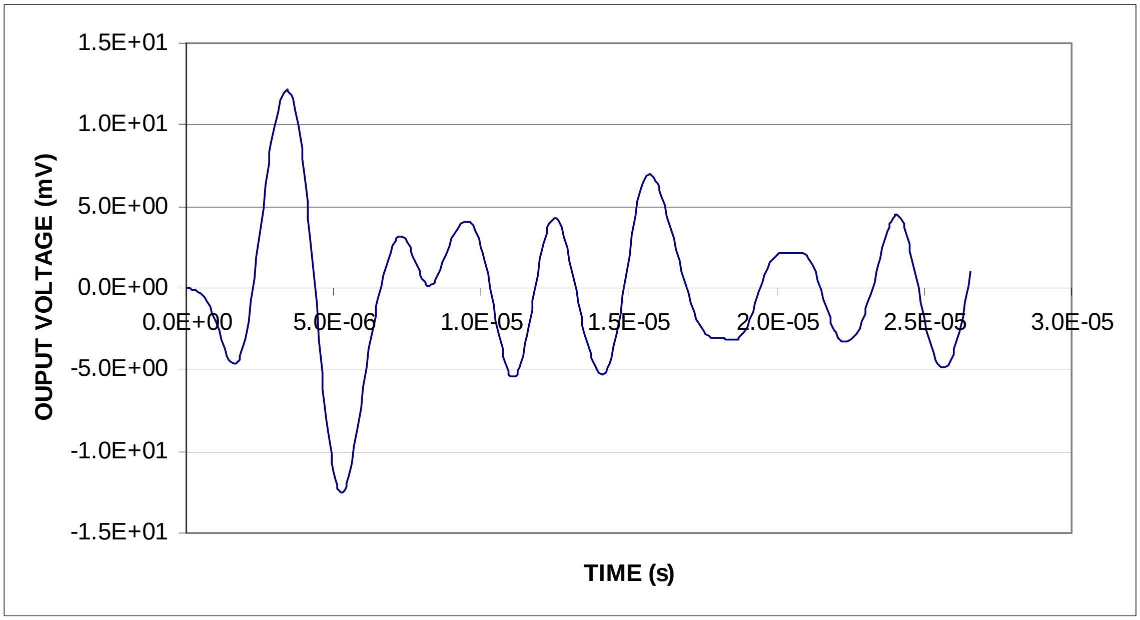

Figure 3.4: Output voltage from the receiving sensor for aluminum

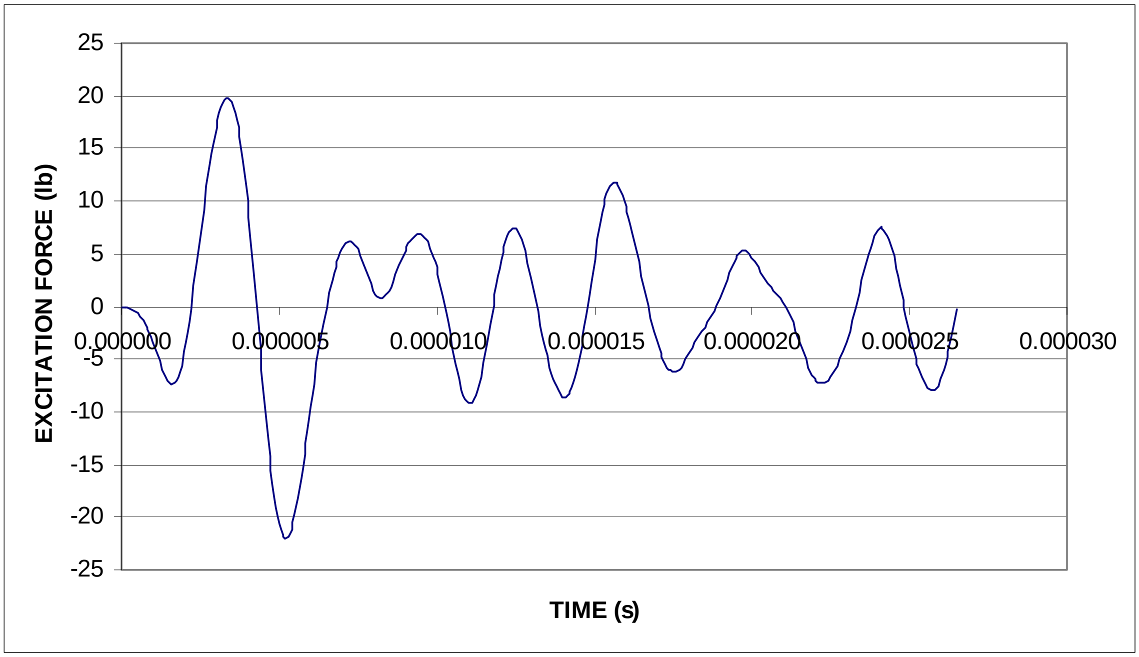

Figure 3.5: Excitation force calculated by the deconvolution process for aluminum

To verify this, the commercial finite element program *ABAQUS Explicit* was used to construct a finite element model of the aluminum block using four-node, axisymmetric, quadrilateral elements with a length of 0.01in. on each side. The material properties were as follows: Young's modulus E=10x10^6psi, Poisson's ratio ν=0.3, density ρ=2.4x10^{-4}lb-s^2/in^4. The forcing function in Figure 3.5 was applied to the model. The calculated normal displacement on the opposite side is shown in Figure 3.6. There is excellent agreement between the finite element results and the measured signal. This verifies that the deconvolution process is accurate, and that the finite element model is adequate for modeling elastic wave propagation through aluminum for the frequencies of interest in our experiments.

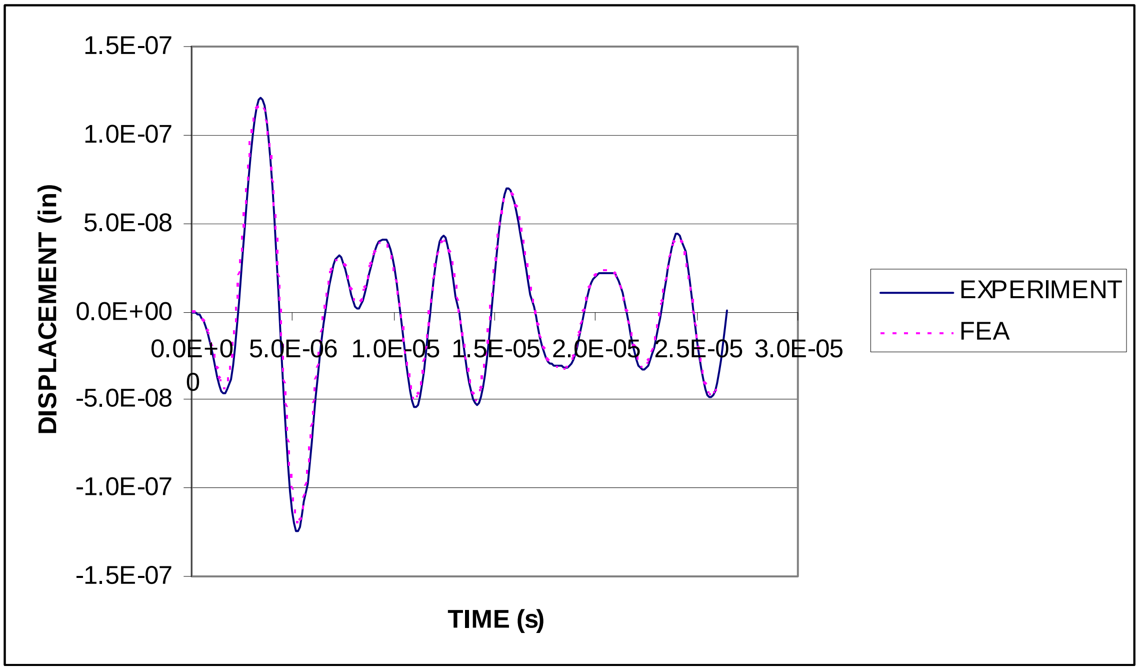

Figure 3.6: Comparison of measured and FEA calculated displacement for aluminum

This experiment was repeated on a 48 in. x 48 in. x14.1 in. block of concrete which can be characterized as having an aggregated gradation of ¾" minus and a minimum compressive strength at 28 days of 3300psi. The test surfaces of the block were prepared by removing rough sections with a hand operated grinding stone. In mounting the sensor in a laboratory grade vacuum grease was used as a compliant between the sensor aperture face and the concrete. A minimum normal force of 4lbs between the sensor and the test block was applied by hand. The input voltage to the excitation sensor was the normal calibration pulse where the energy put to the structure from this pulse is concentrated in the frequency range of 100 to 450 kHz. A Glaser-NIST conical transducer was mounted on the concrete block directly opposite (i.e., 14.1in) from the source. The received signal is shown in Figure 3.7. The deconvolution process was applied to the received signal, and the resulting forcing function is shown in Figure3. 8. This forcing function is of lower frequency and is generally less smooth that that for the aluminum block. This indicates that there may be interaction effects between the wave and the aggregate particles, microcracks and air voids.

Again, a finite element model of the concrete block was constructed using four-node, axisymmetric, quadrilateral elements with a length of 0.01 in. on each side. The forcing function in Figure 3.8 was applied to the model. The calculated normal displacement on the opposite side is shown in Figure 3.9. There is generally good agreement between the finite element results and the measured signal. The FEA results do not quite match the peaks in the experimental results. If needed, this could be improved by refining the mesh. This result verifies that the finite element model is adequate for modeling elastic wave propagation through concrete for the frequencies of interest in our experiments, assuming the concrete behaves as a homogeneous material.

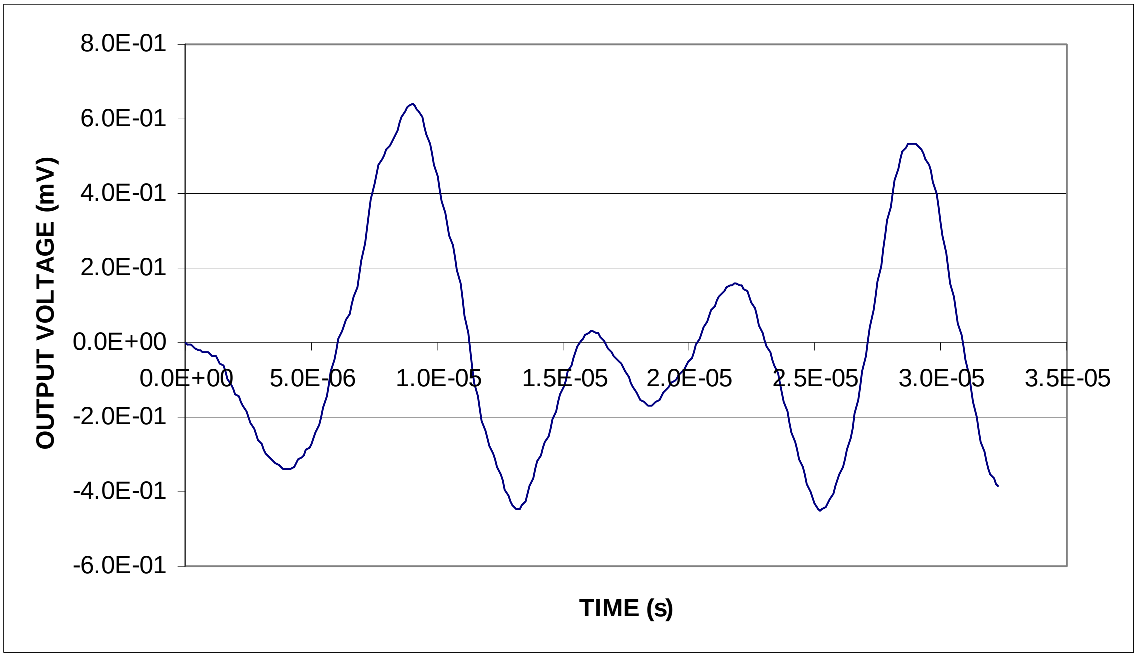

Figure 3.7: Output voltage from the receiving sensor on concrete

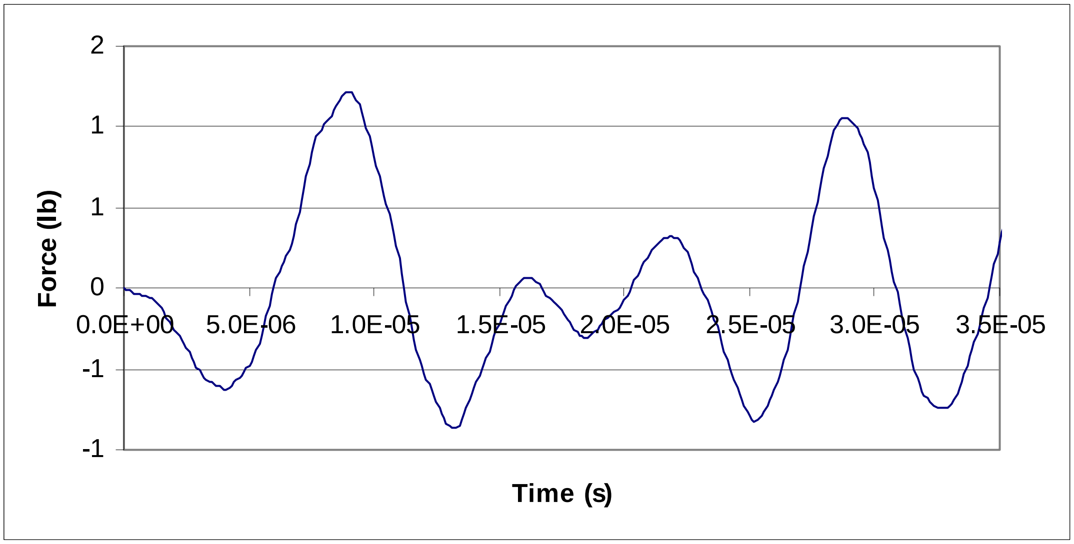

Figure 3.8: Excitation force calculated by the deconvolution process for concrete

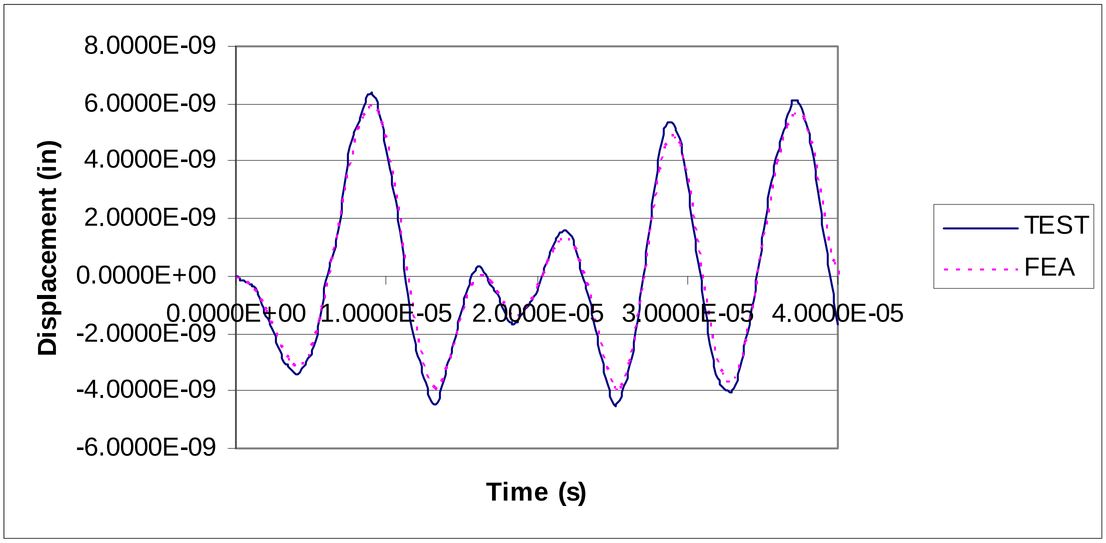

Figure 3.9: Comparison of measured and FEA calculated displacement for concrete

3.2 SURFACE WAVE MODELING

In the previous section we verified that the finite element model is capable of accurately modeling waves transmitted through an elastic solid. In this section we will examine waves along the surface of an elastic solid. We begin by considering a half-space (occupying the space z>0) subjected to a concentrated force normal to the surface at the origin of a cylindrical coordinate system. The boundary conditions are

$$\sigma_{zz} = \frac{\delta(r)}{2\pi r} f(t) \text{ and } \sigma_{zr} = 0 \text{ at z=0} \qquad \textbf{(3-14)}$$

Where f(t) is the time history of the pulse that starts at t=0 and has a duration t_o. The surface displacement in the z-direction for the case where f(t)=H(t), the Heaviside step function, and Poisson's ratio is 1/4, is given by Graf (*1975*) as

$$u_{zH}(r,t) = \frac{1}{32\pi G r}\left\{ \begin{array}{l} A(\tau)[H(\tau-1/\sqrt{3})-H(\tau-1)]+B(\tau)[H(\tau-1)-H(\tau-\gamma)] \\ +12H(\tau-\gamma) \end{array} \right\} \qquad \textbf{(3-15)}$$

Where

$$A(\tau) = 6 - \left(\frac{3}{\tau^2-\frac{1}{4}}\right)^{1/2} - \left(\frac{3\sqrt{3}+5}{\frac{3}{4}+\frac{\sqrt{3}}{4}-\tau^2}\right)^{1/2} + \left(\frac{3\sqrt{3}-5}{-\frac{3}{4}+\frac{\sqrt{3}}{4}+\tau^2}\right)^{1/2} \qquad \textbf{(3-16)}$$

$$B(\tau) = 12 - 2\left(\frac{3\sqrt{3}+5}{\frac{3}{4}+\frac{\sqrt{3}}{4}-\tau^2}\right)^{1/2} \quad \textbf{(3-17)}$$

$$\tau = c_s t / r \quad \textbf{(3-18)}$$

$$\gamma = (3+\sqrt{3})^{1/2}/2 \quad \textbf{(3-19)}$$

As before, the step response (equation (3-15)) can be used to generate the response for f(t) from

$$u_z(r,t) = \int_0^t f'(\xi) u_{zH}(r, t-\xi) d\xi \quad \textbf{(3-20)}$$

Where $f'(\xi)$ is the derivative of $f(\xi)$. Again, making a change of variable, eq (3-6) may be written as

$$u_z(r,t) = \int_0^t f'(t-\zeta) u_{zH}(r,\zeta) d\zeta \quad \textbf{(3-21)}$$

We will consider the case where

$$f(t) = \sin\frac{\pi t}{t_o}\sin\frac{4\pi t}{t_o}[H(t) - H(t-t_o)] \quad \textbf{(3-22)}$$

This pulse is similar in shape to the initial part of the forcing function in Figure 3.8. When $t>t_o$, equation (3-7) gives

$$u_z(r,t) = \int_{t-t_o}^t f'(t-\zeta) u_{zH}(r,\zeta) d\zeta \quad \textbf{(3-23)}$$

Making the change of variable $w=c_d\zeta/r$, equation (3-23) can be written as

$$u_z(r,t) = \int_{c_2(t-t_o)/r}^{c_2 t/r} f'(t - rw/c_d) u_{zH}(r,w) dw \quad \textbf{(3-24)}$$

$$\begin{aligned} 32\pi G r u_z(r,t) = {} & \int_{c_s(t-t_o)/r}^{c_s t/r} f'(t - rw/c_d) A(w)[H(w - 1/\sqrt{3}) - H(w-1)] dw \\ & + \int_{c_s(t-t_o)/r}^{c_s t/r} f'(t - rw/c_d) B(w)[H(w-1) - H(w-\gamma)] dw \end{aligned}$$

$$+12\int_{c_s(t-t_o)/r}^{c_s t/r} f'(t - rw/c_d)H(w-\gamma)dw \tag{3-25}$$

The second integral has a singularity at w=γ when

$$\frac{c_d(t-t_o)}{r} \le \gamma \le \frac{c_d t}{r} \tag{3-26}$$

The integrals will be evaluated numerically. The problem of dealing with the singularity can be handled by subtracting out the singularity in the following manner (*Kantorovich 1934*). Consider an integral of the form

$$I = \int_{x_1}^{x_2} \frac{F(x)}{\sqrt{x_2^2 - x^2}} dx \tag{3-27}$$

Which has a singularity at the upper limit. This can be re-written as

$$I = \int_{x_1}^{x_2} \frac{F(x_2)}{\sqrt{x_2^2 - x^2}} dx + \int_{x_1}^{x_2} \frac{F(x) - F(x_2)}{\sqrt{x_2^2 - x^2}} dx \tag{3-28}$$

The first integral has a singularity but can be evaluated in closed form. Thus,

$$I = F(x_2)\left(\frac{\pi}{2} - \sin^{-1}\frac{x_1}{x_2}\right) + \int_{x_1}^{x_2} \frac{F(x) - F(x_2)}{\sqrt{x_2^2 - x^2}} dx \tag{3-29}$$

The second integral contains no singularity and can be evaluated numerically using standard methods.

An analysis was performed for a concrete block with t_o=20x10^{-6}s. The shape of the input pulse is shown in Figure 3.10.

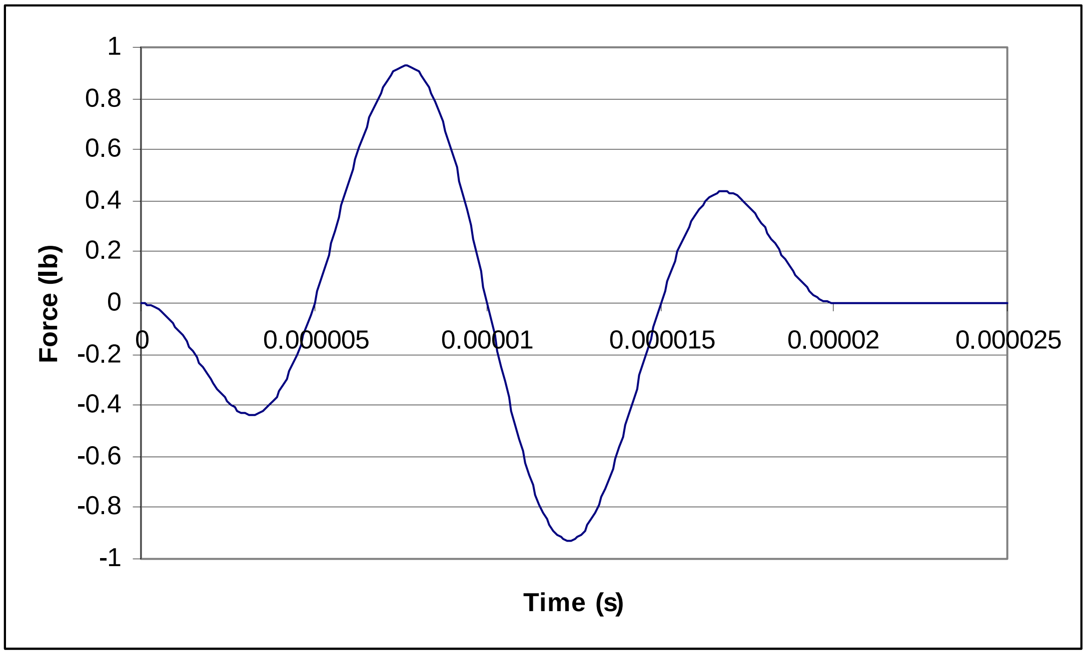

Figure 3.10: Input pulse for surface wave calculation

A finite element analysis was performed for this case using a model similar to the one described in the previous section. The response from the analytical solution is compared to the finite element results at a position 3 in. for the source in Figure 3.11. There is excellent agreement between the two. This demonstrates that the finite element model is adequate for modeling elastic wave propagation along the surface of a body for frequencies of interest in our experiments.

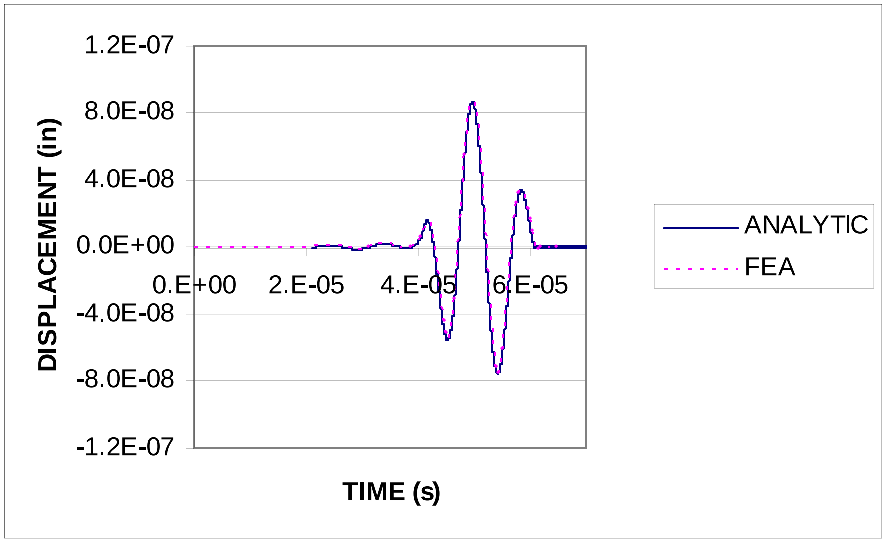

Figure 3.11: Comparison of analytical and FEA solutions for a surface wave

4.0 WAVE PROPAGATION TESTING AND ANALYSIS OF CONCRETE

This section describes wave propagation testing and finite element analysis of un-reinforced concrete and concrete reinforced with steel bars.

4.1 UN-REINFORCED CONCRETE

Tests were performed on a 48 in. x 48 in.x14.1 in. block of un-reinforced concrete as described in the previous section. The test set-up is shown in Figure 4.1. The calibration pulse described in the previous section was sent to the excitation sensor. In the first test the receiver sensor was mounted on the reverse face directly opposite to the excitation sensor (position x=0 inches). The test was repeated nine times with the receiver sensor moved in 1 inch increments away from the original position (position x=1,2,…..9 inches). The output of the receiver sensor is shown in Appendix A for each of the positions. A finite element analysis of the block using the forcing function in Figure 3.8 was performed. The calculated vertical displacement for each position is shown in Appendix B.

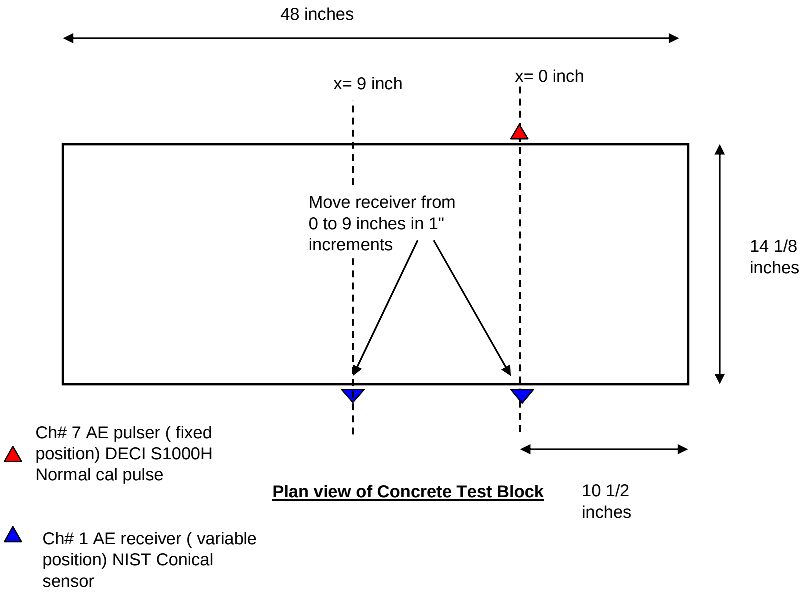

Figure 4.1: Test set-up for wave propagation in an un-reinforced concrete block

Figure 4.2 shows the test measured pulse at position x=0 in. Figure 4.3 shows the FEA calculated pulse at x=0 in. It is not possible to make a direct comparison of the experimental and FEA results. The typical experimental response wave form begins with some minor oscillations followed by a negative peak in the 0-5 microsecond time frame followed by a larger positive peak in the 5-10 microsecond time frames. A plot of the normalized amplitude of the first positive peak as a function of x position is shown in Figure 4.4 from both the measured and calculated waveforms. It is expected that the magnitudes of these peaks would decrease monotonically with increasing x-position due to geometric attenuation and changing angle of incidence. The fact that this does not happen in the test results indicates that there may be scattering due to wave-aggregate particle, mircrocrack and air void interaction. Large variations in p-wave amplitudes were also realized in similar work performed by Shumacher (*2008*). Therefore, the experiment and FEA results will be compared by first normalizing the response relative to the magnitude of the first positive peak (i.e., the amplitude of this peak is made equal to one). Also, the FEA results have been shifted in time to align the experiment and FEA first positive peaks. Comparison of experiment and FEA results are shown in Figures. 4.5 to 4.14 for each position. As expected, the agreement between experiment and FEA results is generally good for the first period of oscillation. After that, the agreement generally deteriorates with increasing x-position. The period of oscillation appears to broaden with increasing x-position in the experimental results. This does not occur in the FEA results.

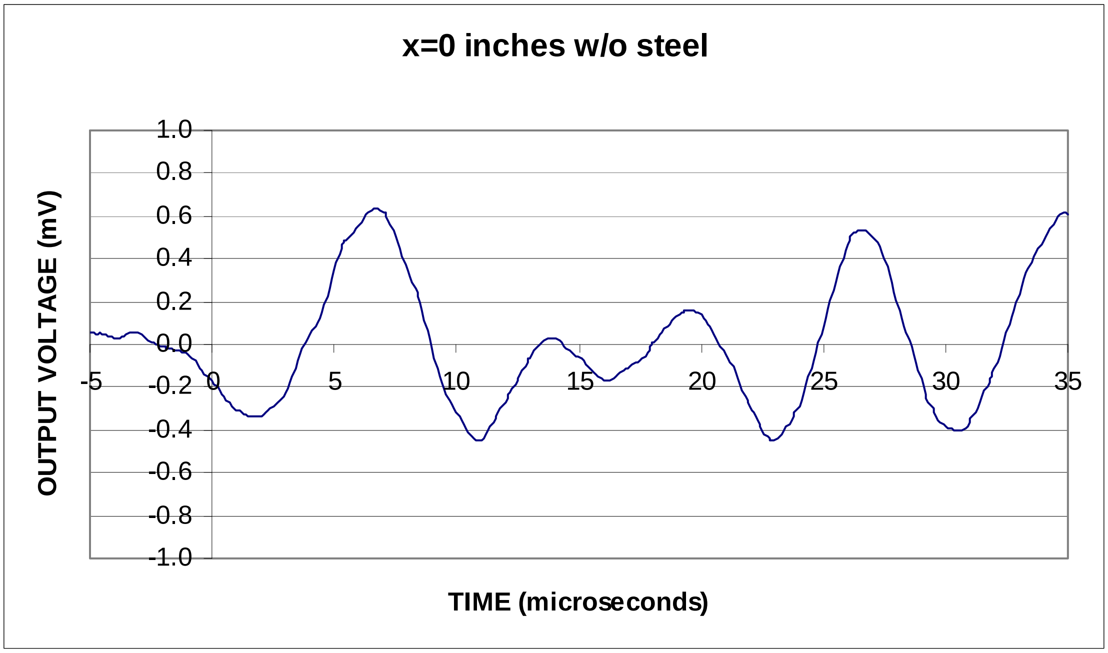

Figure 4.2: Receiver sensor output in the un-reinforced concrete block at position x=0 inches

Figure 4.3: FEA results for the un-reinforced concrete block at position x=0 inches

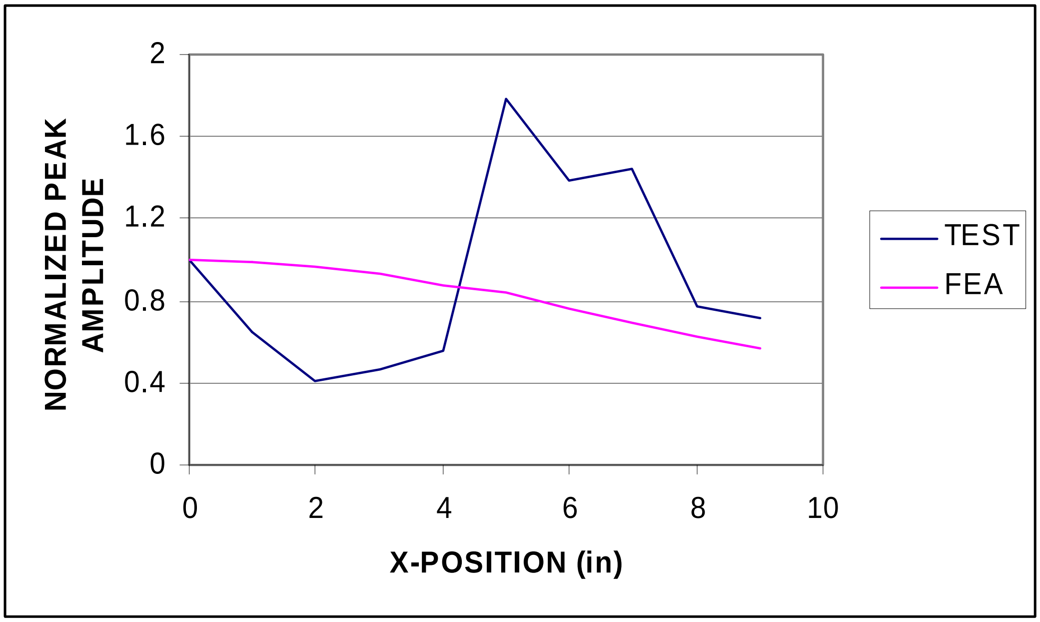

Figure 4.4: Comparison of normalized peak wave amplitude versus x-position

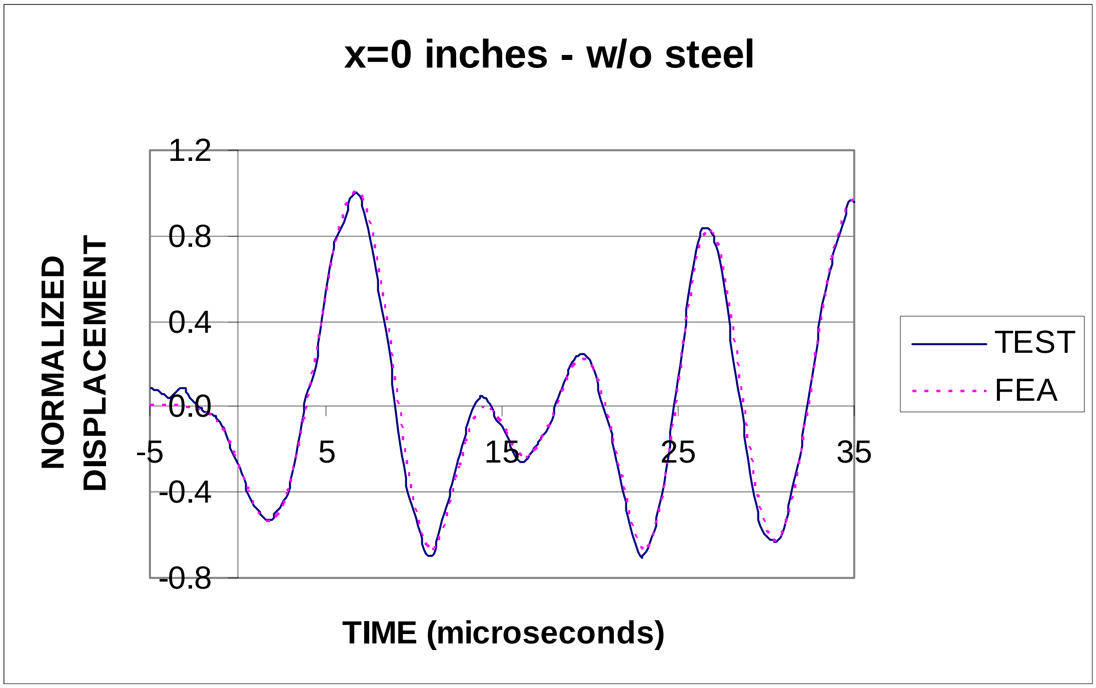

Figure 4.5: Comparison of test and FEA results for un-reinforced concrete at x=0 inches

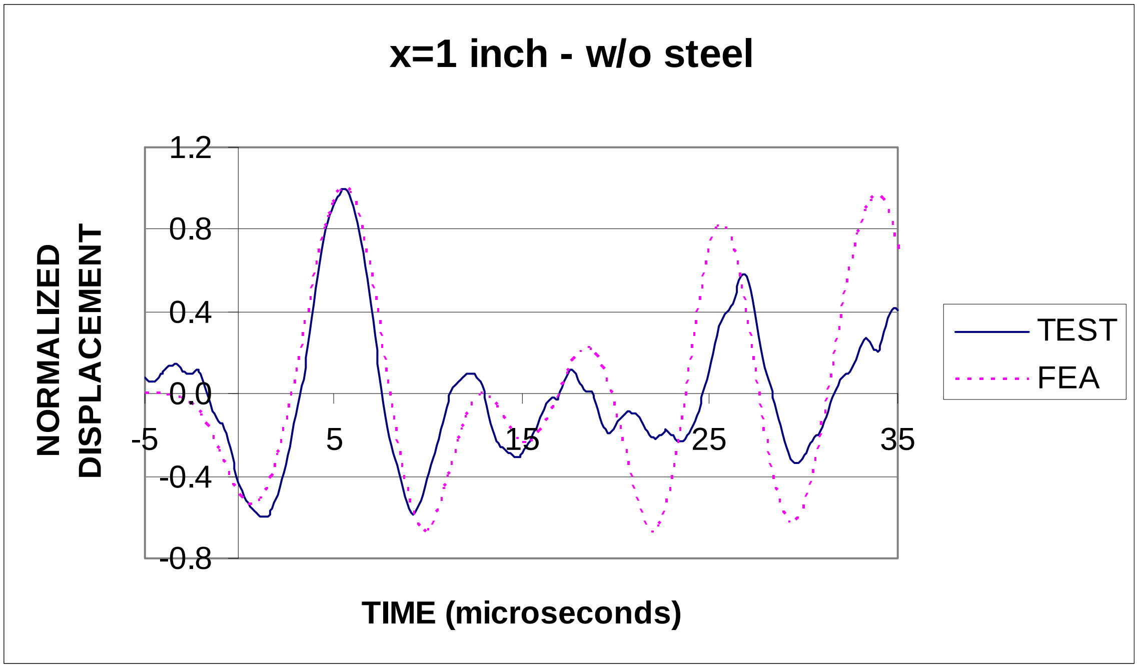

Figure 4.6: Comparison of test and FEA results for un-reinforced concrete at x=1 inch

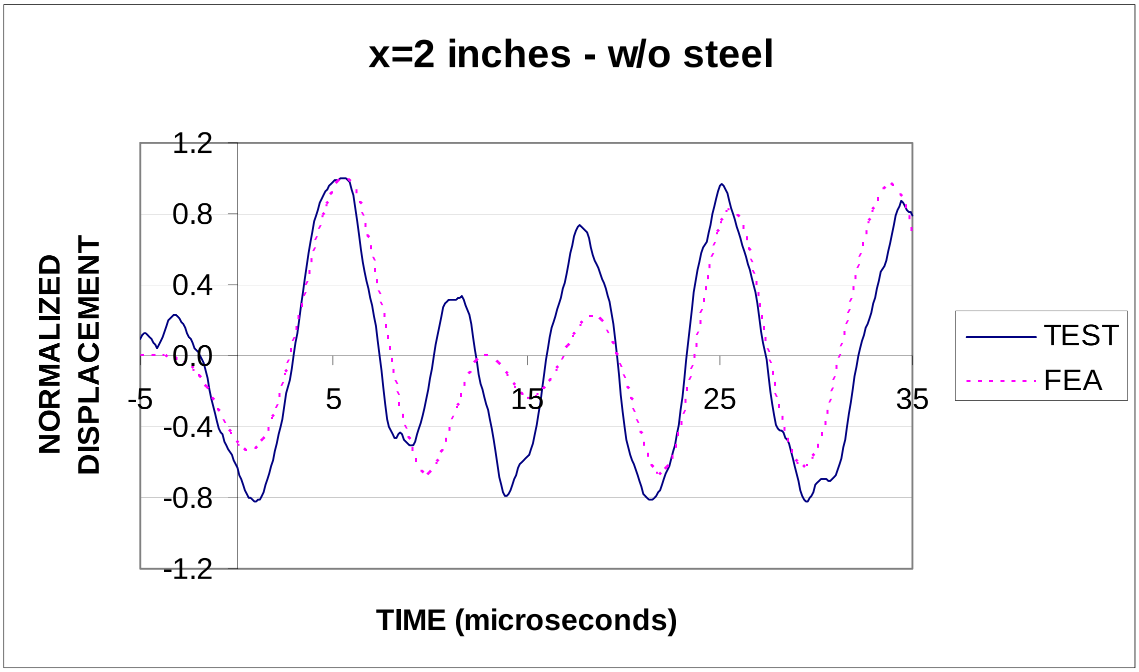

Figure 4.7: Comparison of test and FEA results for un-reinforced concrete at x=2 inches

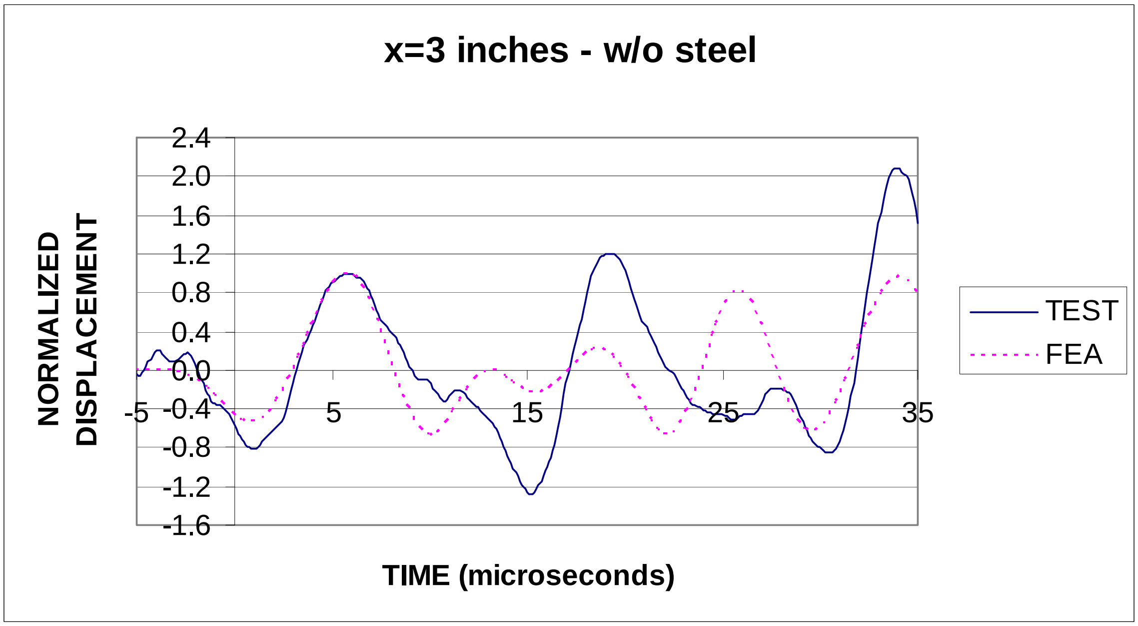

Figure 4.8: Comparison of test and FEA results for un-reinforced concrete at x=3 inches

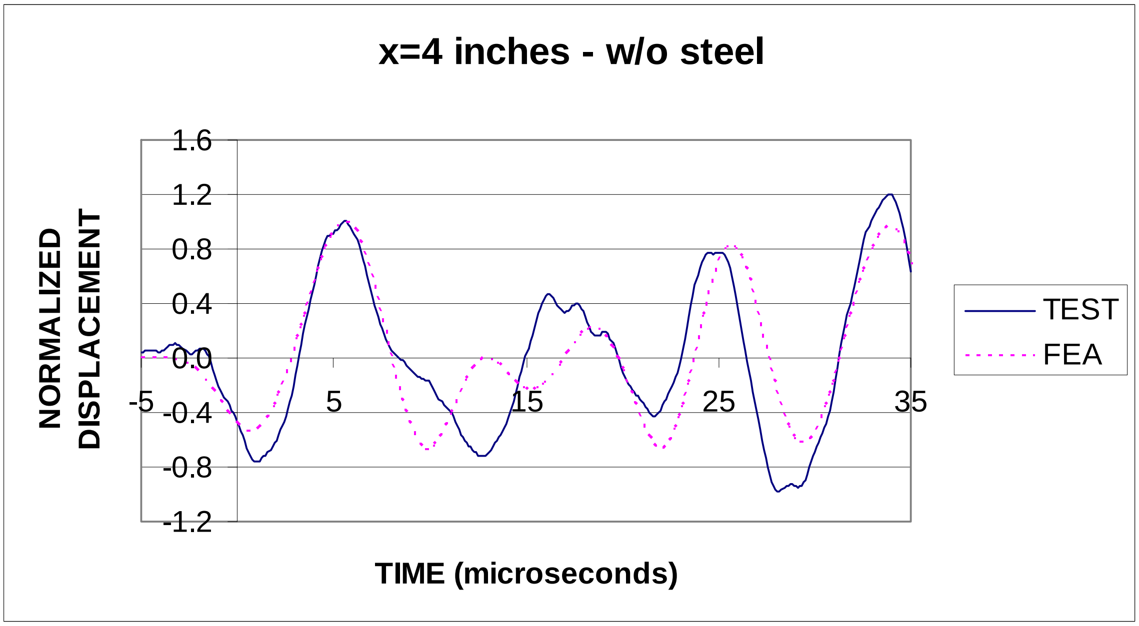

Figure 4.9: Comparison of test and FEA results for un-reinforced concrete at x=4 inches

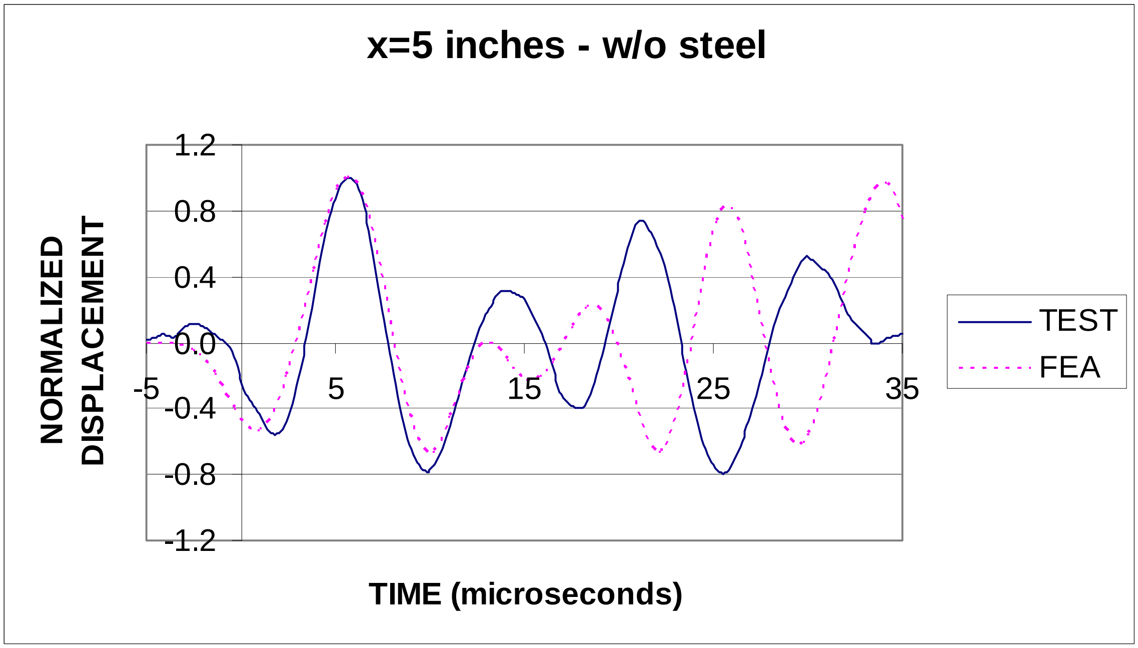

Figure 4.10: Comparison of test and FEA results for un-reinforced concrete at x=5 inches

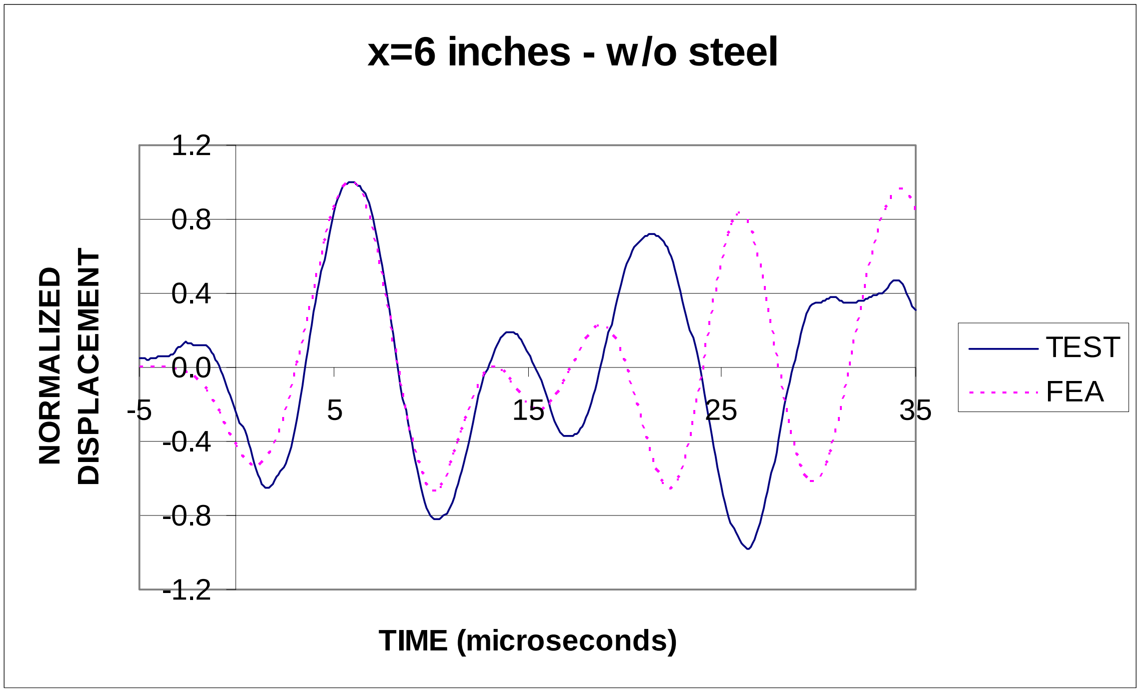

Figure 4.11: Comparison of test and FEA results for un-reinforced concrete at x=6 inches

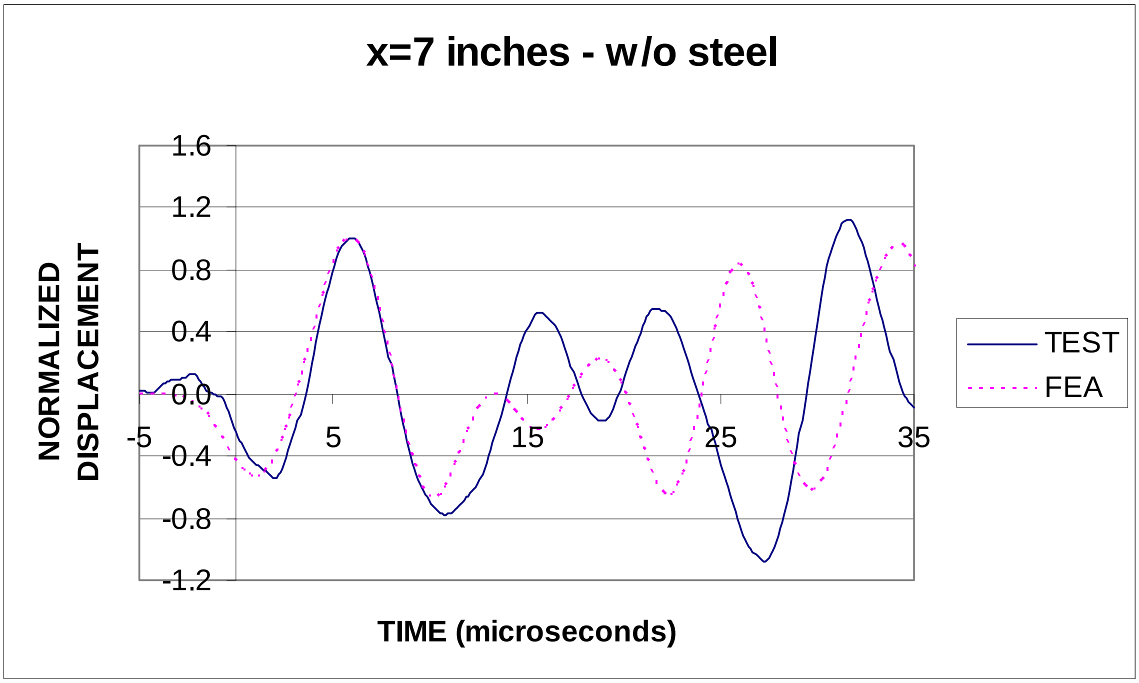

Figure 4.12: Comparison of test and FEA results for un-reinforced concrete at x=7 inches

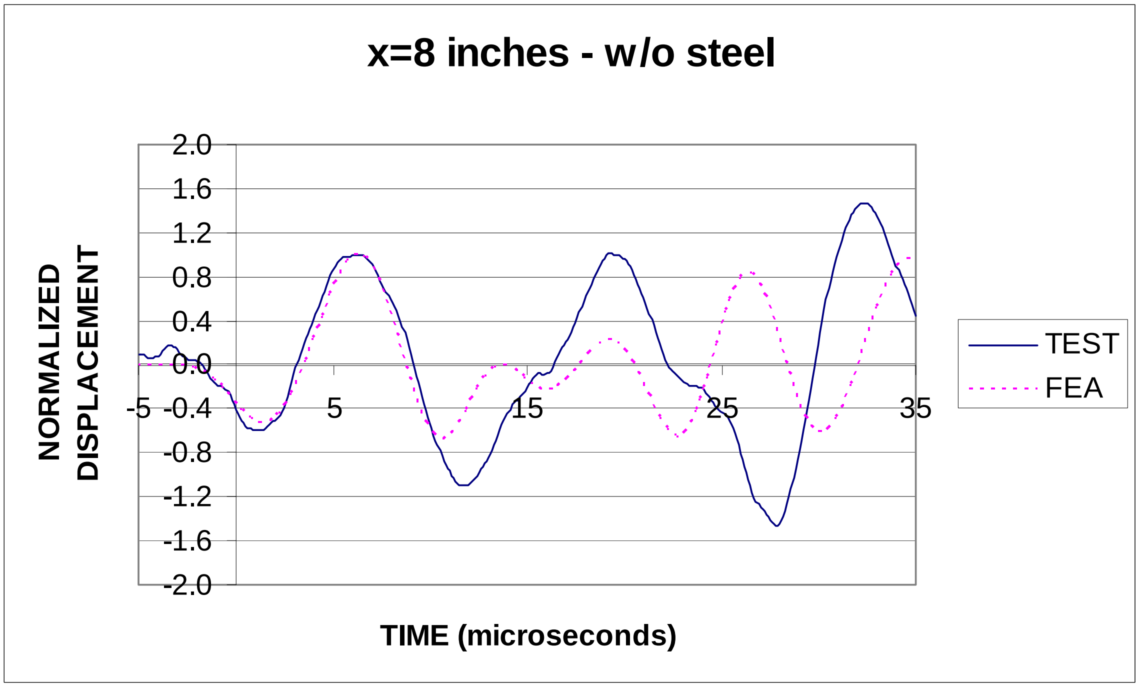

Figure 4.13: Comparison of test and FEA results for un-reinforced concrete at x=8 inches

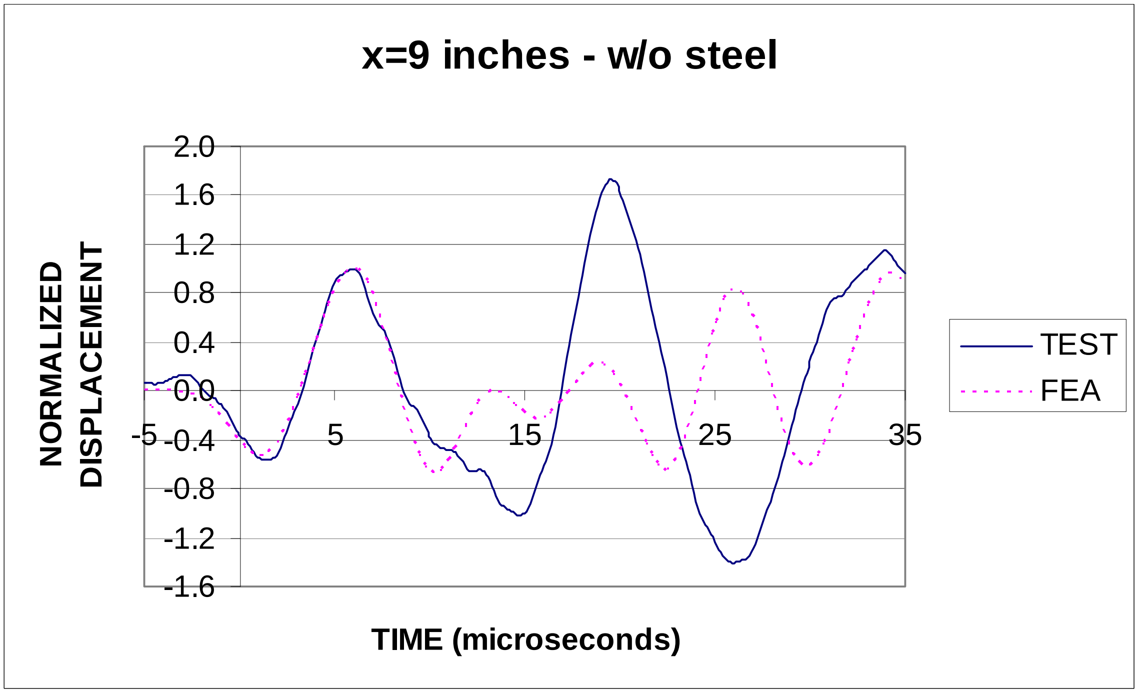

Figure 4.14: Comparison of test and FEA results for un-reinforced concrete at x=9 inches

4.2 REINFORCED CONCRETE

The tests described in the previous section were repeated on a 48inx48inx14.1in block of concrete containing 0.5 in. diameter steel reinforcement bars. The test set-up is shown in Figure 4.14. There are two rows of bars with their centers 2.25 in. below each surface. The horizontal spacing between the centers of each of the bars is 6 in. The presence of the steel reinforcing bars could cause some complex scattering and reflecting of the waves for both the test and FEA results. The output of the receiver sensor is shown in Appendix C for each of the x-positions. Again, a finite element analysis of the block, this time including reinforcing steel, using the forcing function in Figure 3.8 was performed. The calculated vertical displacement for each position is shown in Appendix D. Figure 4.15 shows a plot of normalized first peak amplitude versus x-position from the test and FEA results. There is some qualitative similarity between the test and FEA results in that they both exhibit a significant drop in amplitude in the vicinity of the reinforcing bar, as expected.

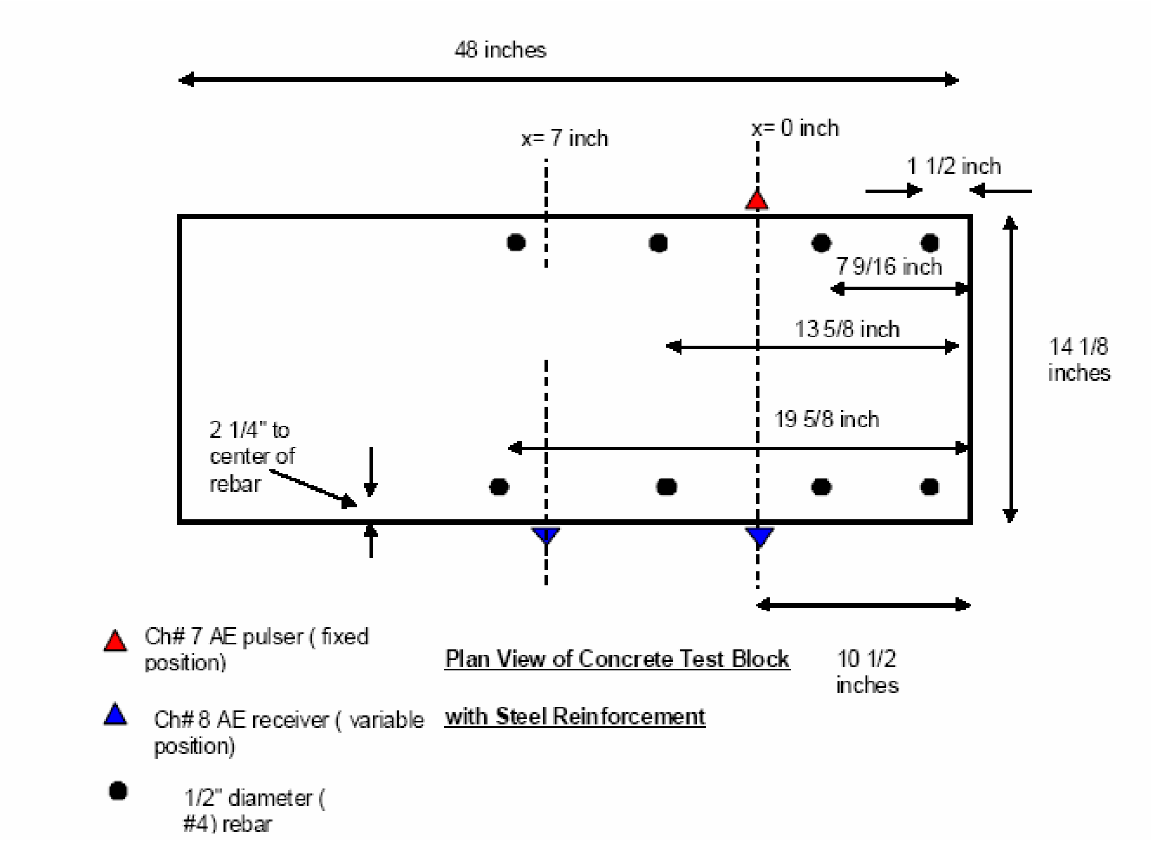

Figure 4.14: Schematic of the test setup for pulses through a steel reinforced concrete block

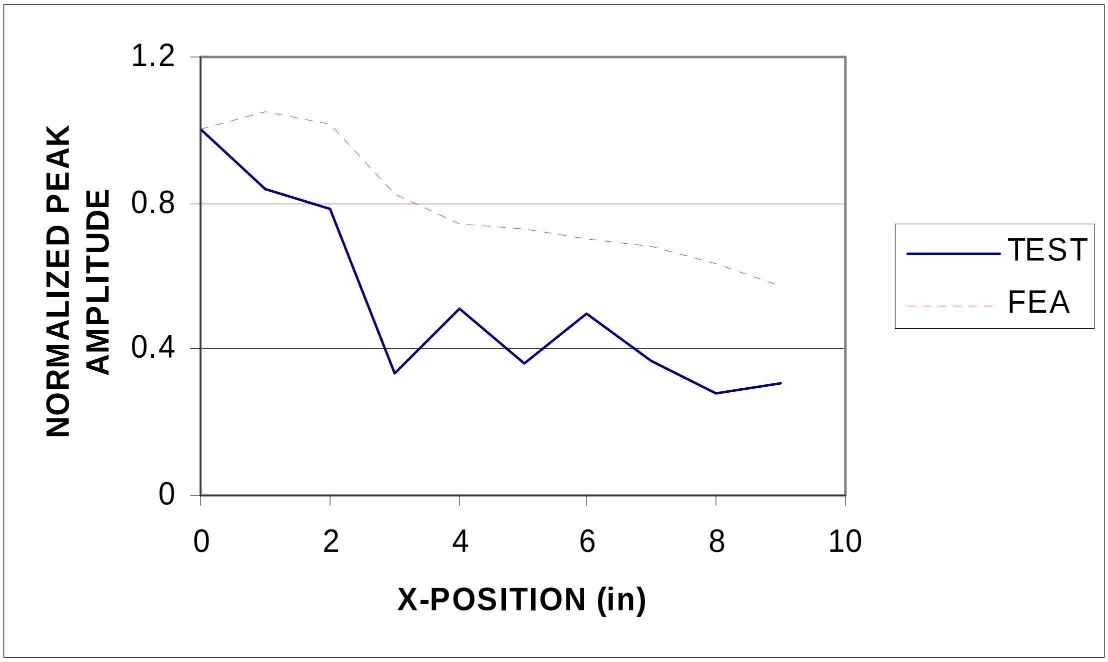

Figure 4.15: Comparison of normalized peak wave amplitude versus x-position

As before, the experiment and FEA results were compared by first normalizing the response relative to the magnitude of the first positive peak (i.e., the amplitude of this peak is made equal to one), and the FEA results were shifted in time to align the experiment and FEA first positive peaks. Comparison of experiment and FEA results are shown in Figures. 4.15 to 4.24 for each position. As was the case for not reinforced concrete, the agreement between test results and FEA results deteriorates with increasing x-position for secondary p-wave oscillations. However, the arrival and magnitude of the first p-wave oscillations are in relatively good agreement between the FEA and experimental results. The period of oscillation appears to broaden with increasing x-position in the test results, but not in the FEA results.

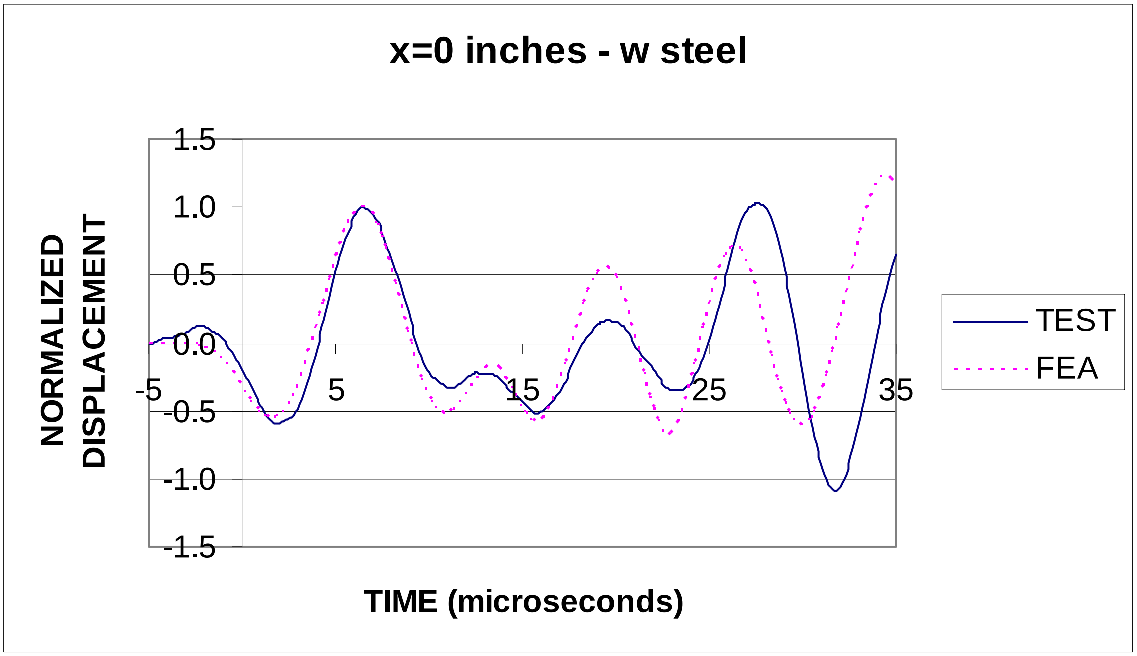

Figure 4.16: Comparison of test and FEA results for reinforced concrete at x=0 inches

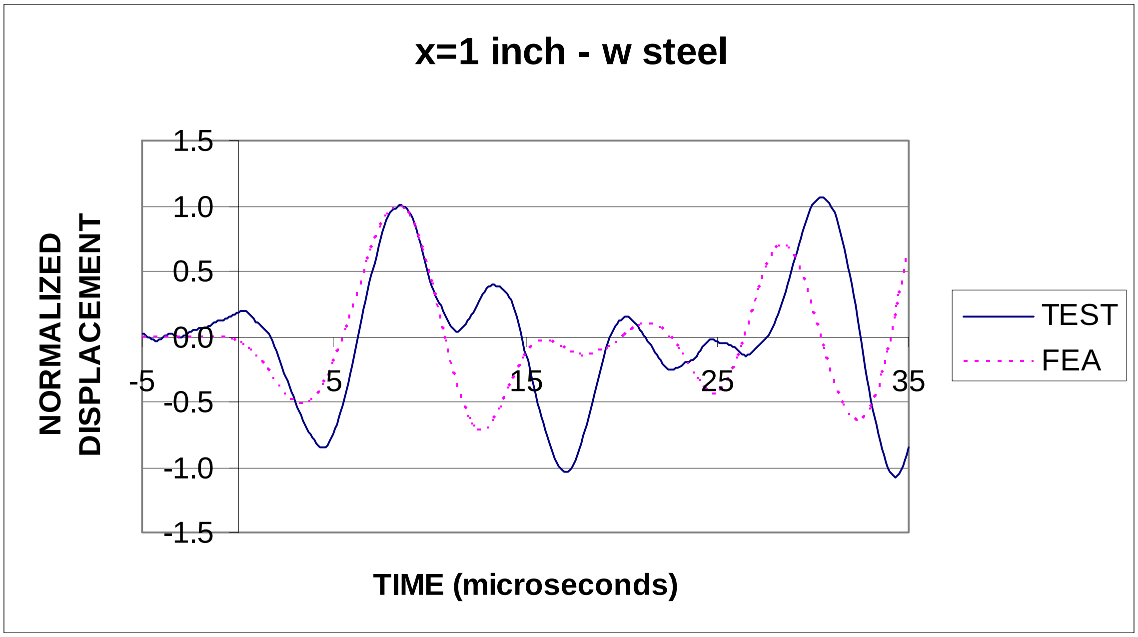

Figure 4.17: Comparison of test and FEA results for reinforced concrete at x=1 inch

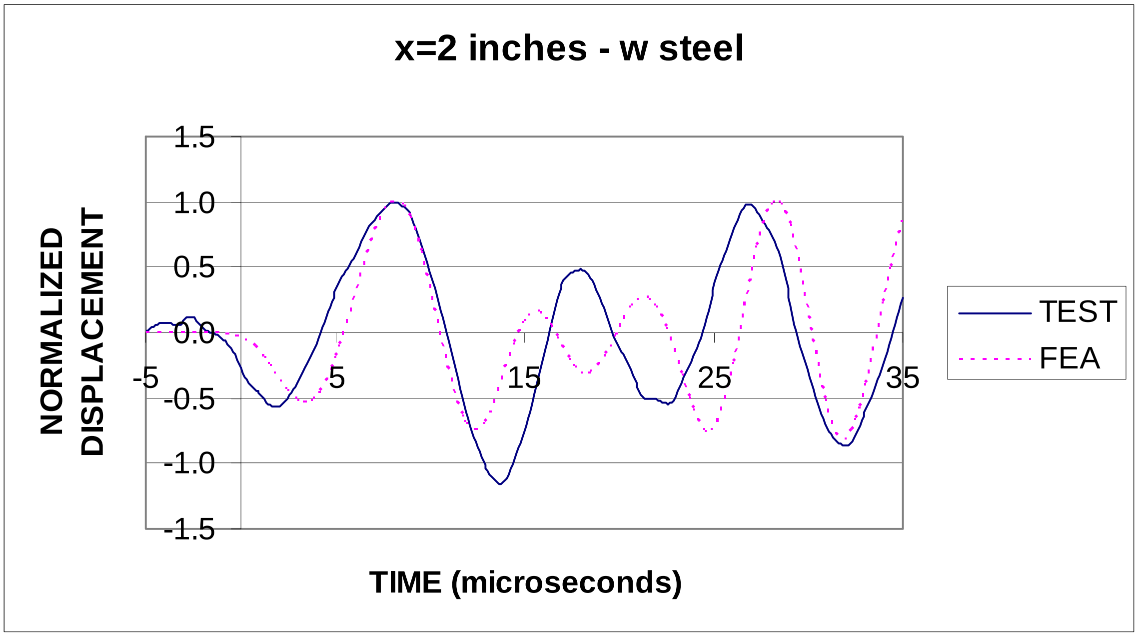

Figure 4.18: Comparison of test and FEA results for reinforced concrete at x=2 inches

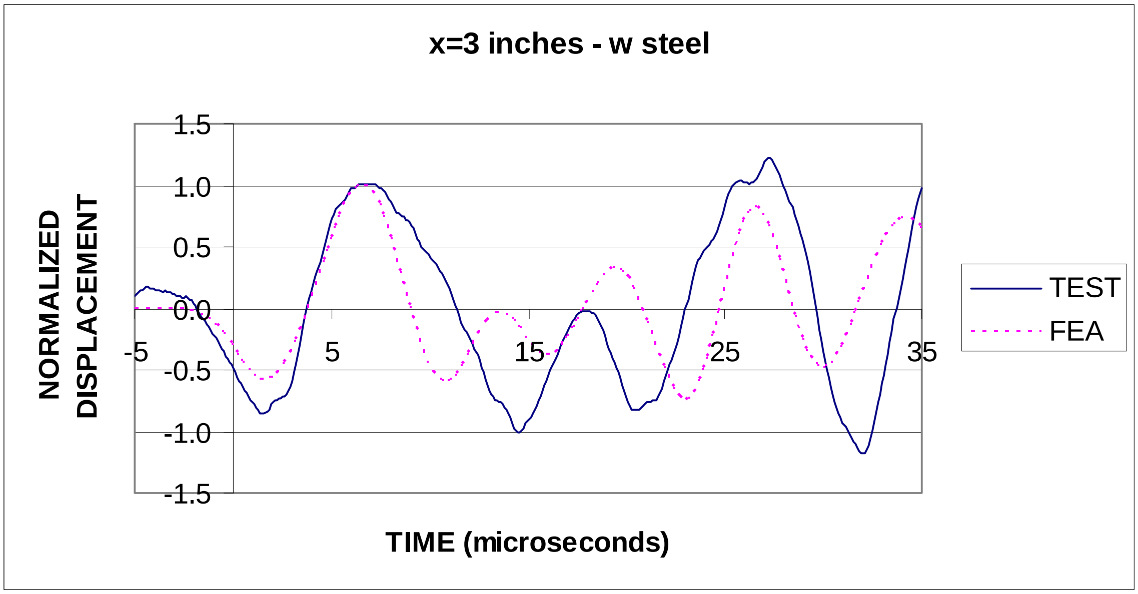

Figure 4.19: Comparison of test and FEA results for reinforced concrete at x=3 inches

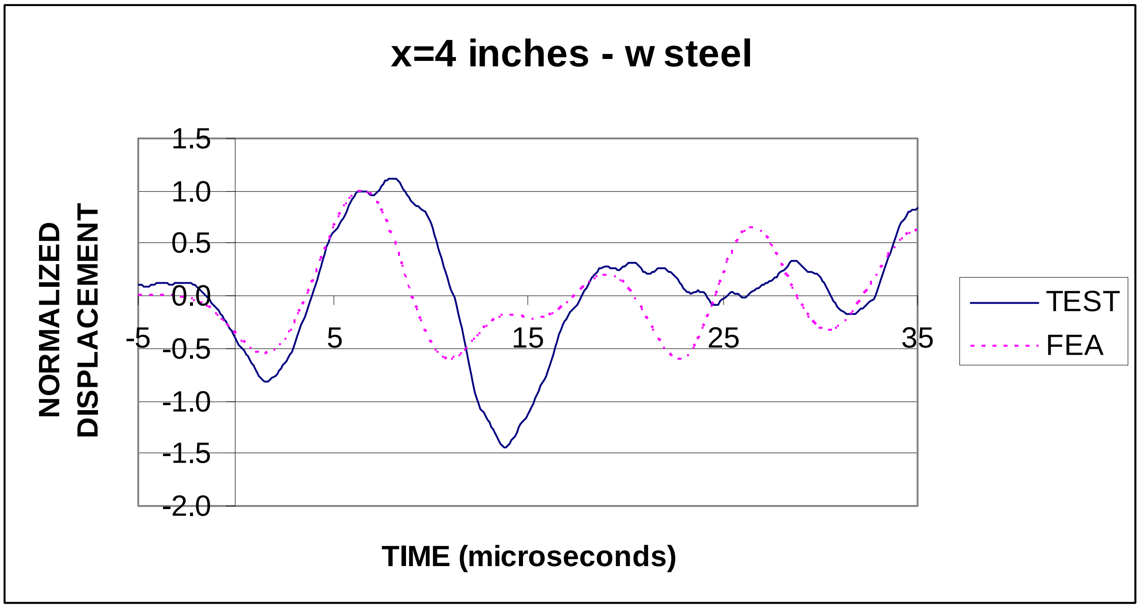

Figure 4.20: Comparison of test and FEA results for reinforced concrete at x=4 inches

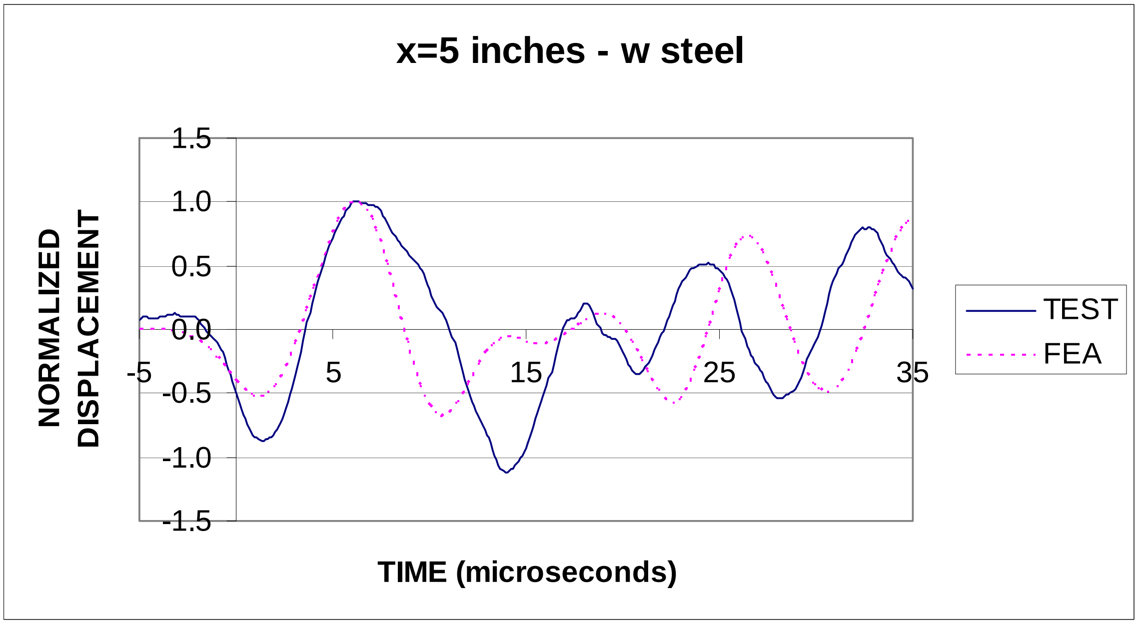

Figure 4.21: Comparison of test and FEA results for reinforced concrete at x=5 inches

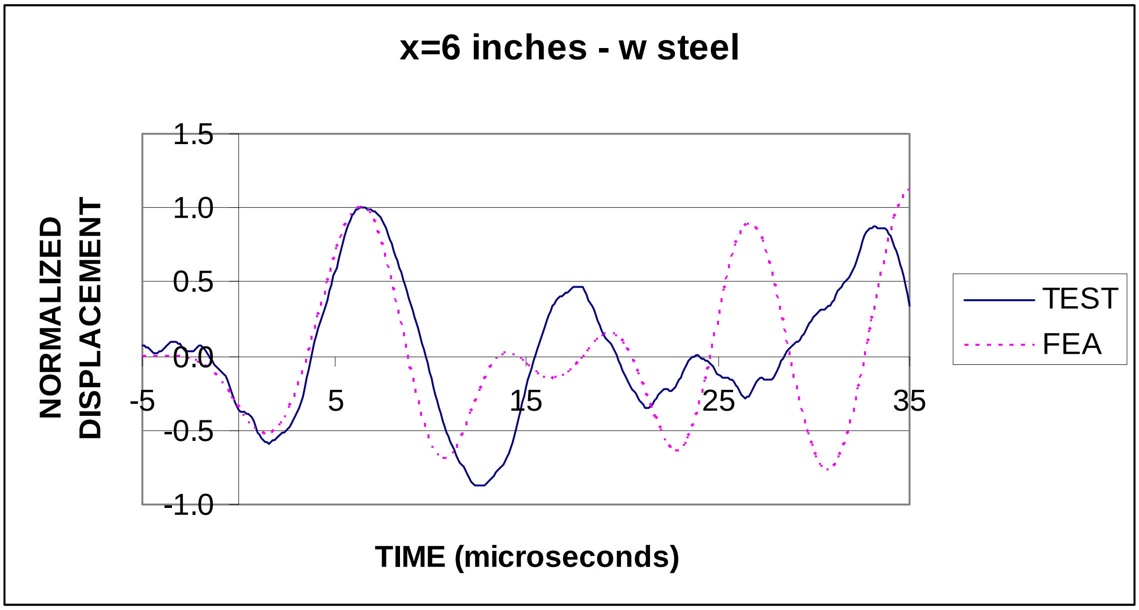

Figure 4.22: Comparison of test and FEA results for reinforced concrete at x=6 inches

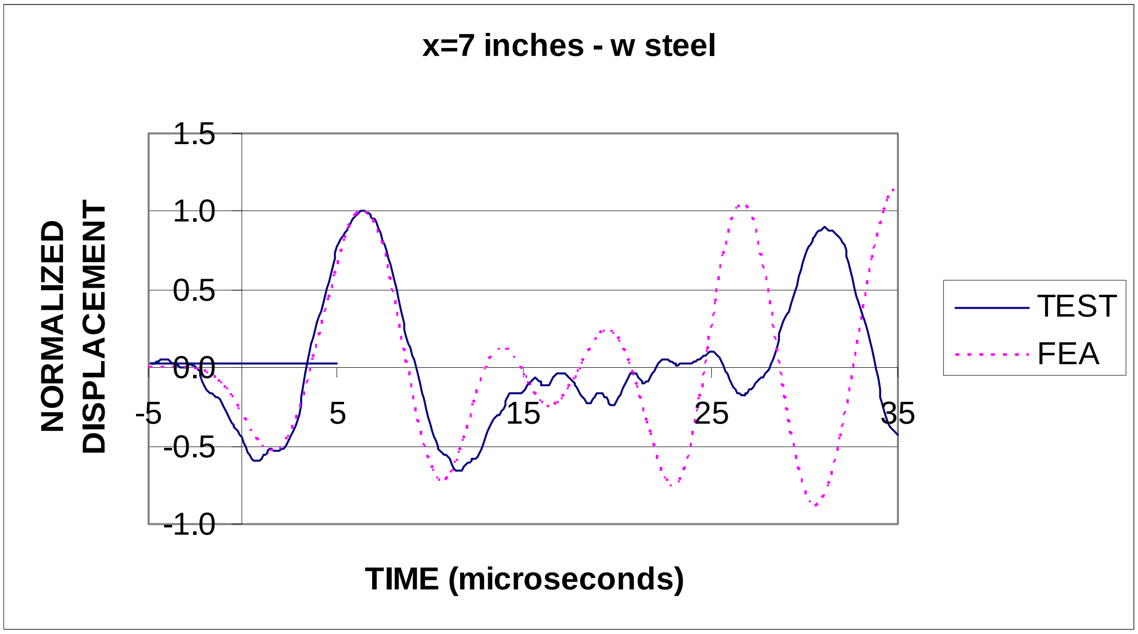

Figure 4.23: Comparison of test and FEA results for reinforced concrete at x=7 inches

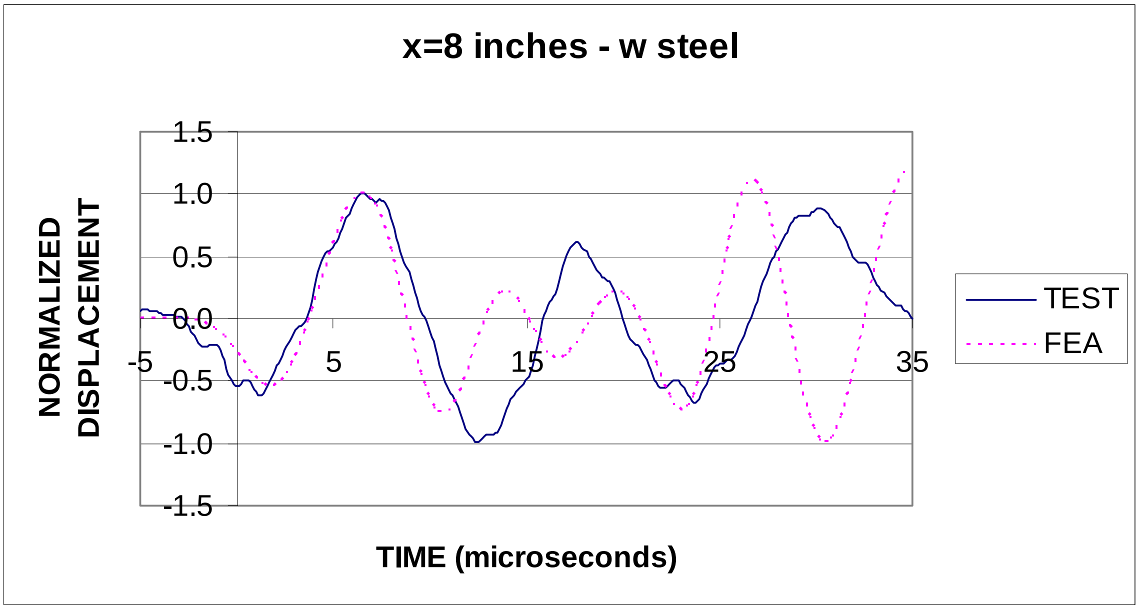

Figure 4.24: Comparison of test and FEA results for reinforced concrete at x=8 inches

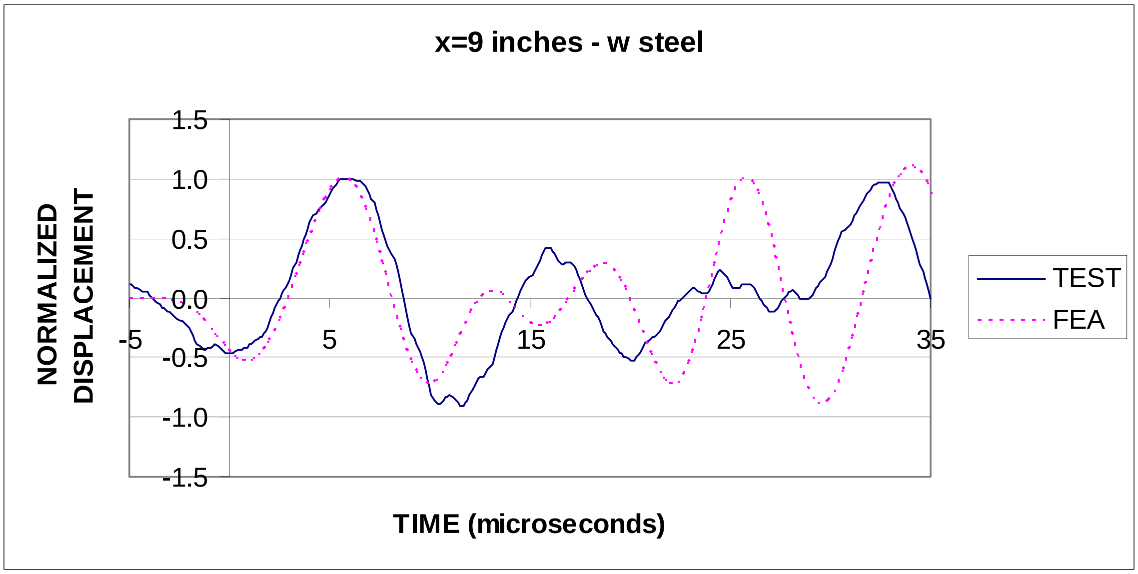

Figure 4.25: Comparison of test and FEA results for reinforced concrete at x=9 inches

5.0 CONCLUSION

The objective of this project was to evaluate the capability of finite element analysis to accurately simulate the propagation of stress waves through reinforced concrete. This was done by performing some very basic stress wave propagation tests on both not reinforced and reinforced concrete specimens and by comparing the test results to computer predictions. Before making this comparison, the finite element model was validated by comparing its predictions to those generated from analytical solutions. It was determined that the finite element model gave very accurate results for waves propagating at frequencies of interest in our tests. Reasonable agreement between the FEA and experimental results was found for the first p-wave oscillation. Unfortunately, the agreement between test results and finite element predictions after the first oscillation was generally not very good for both not reinforced and reinforced concrete. The reason for this appears to be the fact that the finite element model treats the concrete as a homogeneous medium and ignores the effects of property differences between the cement, aggregate, microcracks and air voids. The test results tended to exhibit a much more complex and unpredictable behavior than that in the finite element model. This complex response appears to be most likely the result of scattering of waves as they interact with the non-homogenities discussed above. It is possible that this behavior could be simulated if statistical properties of the size and distribution of particles in the concrete could be determined and then applied to a finite element mesh. However, such an endeavor was beyond the scope of the current project.

The primary purpose of performing FEA on such structures is to quantify the Green's function of the structure which is required for performing quantitative AE analyses. The two most useful forms of such analysis being source location and moment tensor inversion only require tracking the first p-wave oscillation (*Schumacher 2008*). Thus even with the added complications of material non-homogenity found in concrete, using FEA to quantify the Green's function of steel reinforced concrete structures can be both practical and useful.

6.0 REFERENCES

Flugge, W., *Viscoelasticity*, Blaisdell, London, 1967, pp. 22-29.

Graff, K.F., *Wave Motion in Elastic Solids*, Dover Publications, New York, 1975, pp.356-368.

Kantorovich, L.V., “On approximate calculation of certain types of definite integrals and other applications of the method of removal of singularities,” *Mat Sbornik*, Vol. 41, 1934, pp. 235-245.

Knopoff, L., “Surface motions of a thick plate,” *Journal of Applied Physics*, Vol. 29, 1958, pp. 661-670.

Landis, E. N., and Shah, S.P., “Frequency dependent stress wave attenuation in cement-based materials,” *Journal of Engineering Mechanics*, Vol., 1995, pp. 737-743.

Lovejoy, S. C., “Development of acoustic emissions testing procedures applicable to conventionally reinforced concrete deck girder bridges subjected to diagonal tension cracking,” Ph. D Dissertation, Department of Mechanical Engineering, Oregon State University, 2006.

Schumacher, T., Higgins, C., Lovejoy, S.C., Guidelines for Practical Acoustic Emission Testing of Vintage RCDG Highway Bridges, SPR-633.

Sinha, N.K. and Kuszta, B., *Modeling and Identification of Dynamic Systems*, Van Nostrand, New York, 1983, pp. 13-15.

Wu, T.T., Fang, J.S., Liu, G.Y., and Kuo, M.K., “Determination of elastic constants of a concrete specimen using transient elastic waves,” Journal *of the Acoustical Society of America*, Vol. 98, 1995, pp. 2142-2148.

APPENDIX A

The sensor output from the tests described in section 4.1 is presented here.

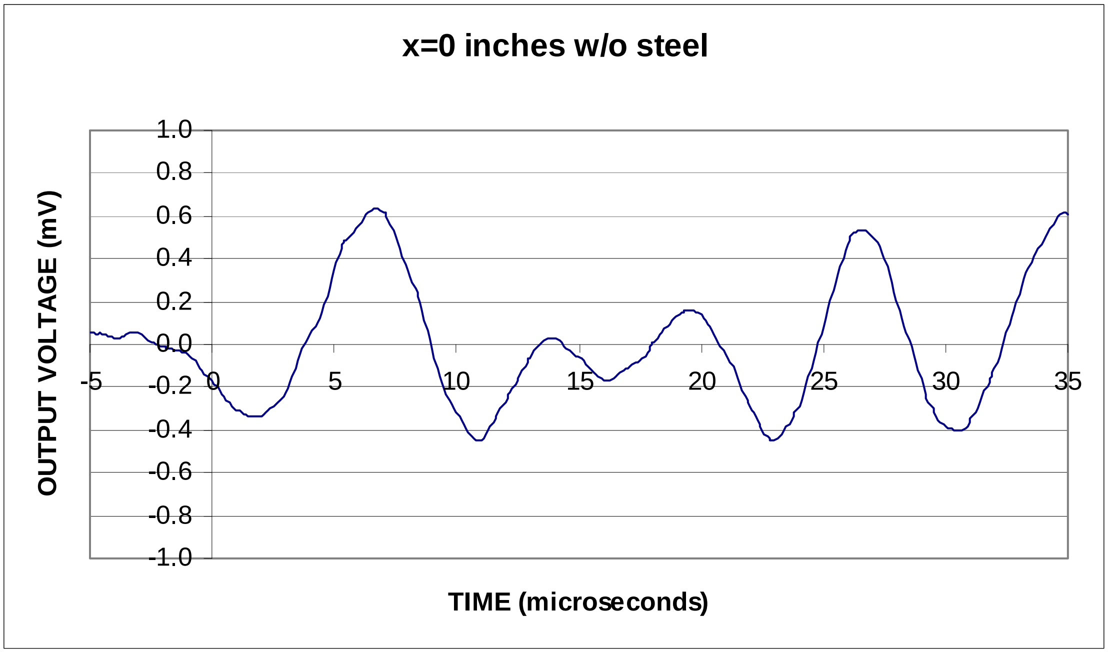

Figure A.1: Receiver sensor output in the un-reinforced concrete at position x=0 inches

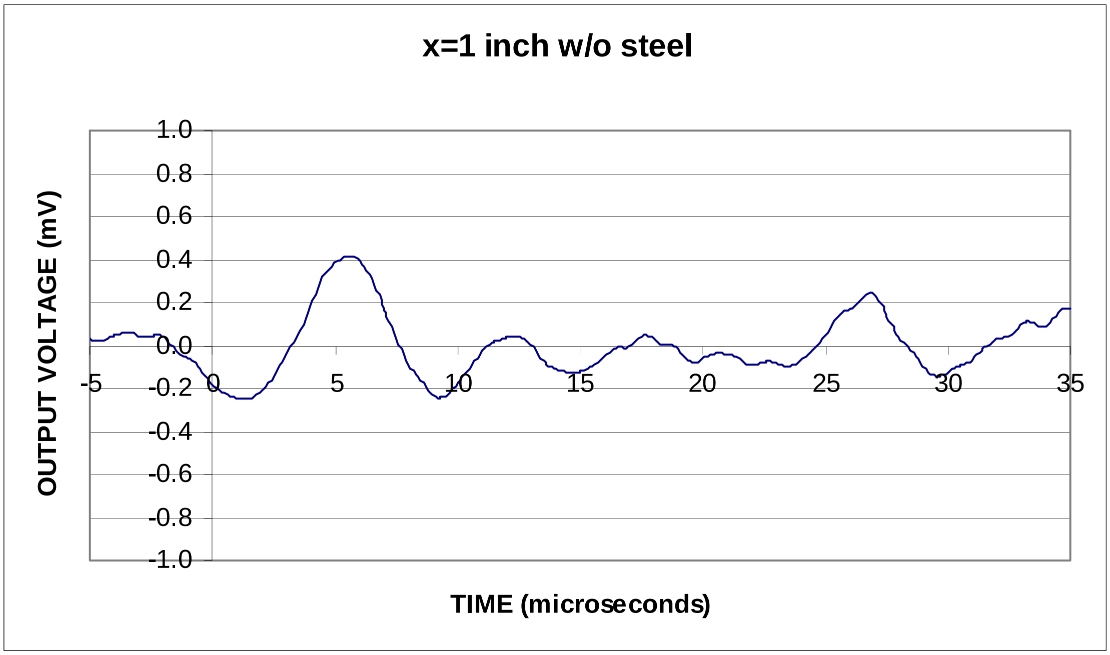

Figure A.2: Receiver sensor output in the un-reinforced concrete block at position x=1 inch

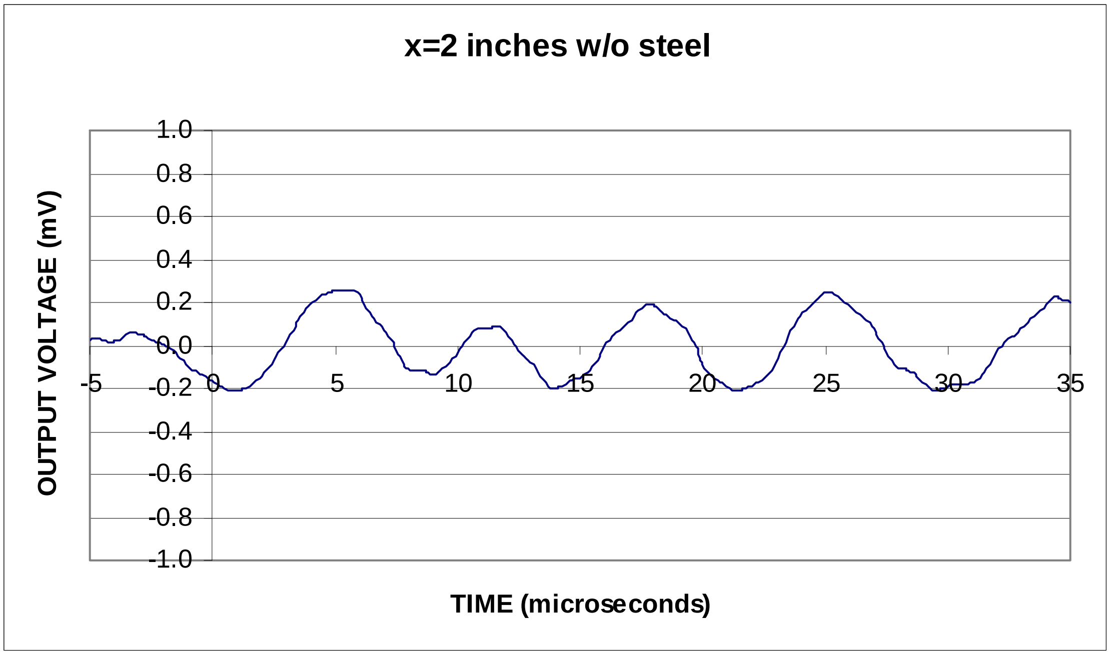

Figure A.3: Receiver sensor output in the un-reinforced concrete at position x=2 inches

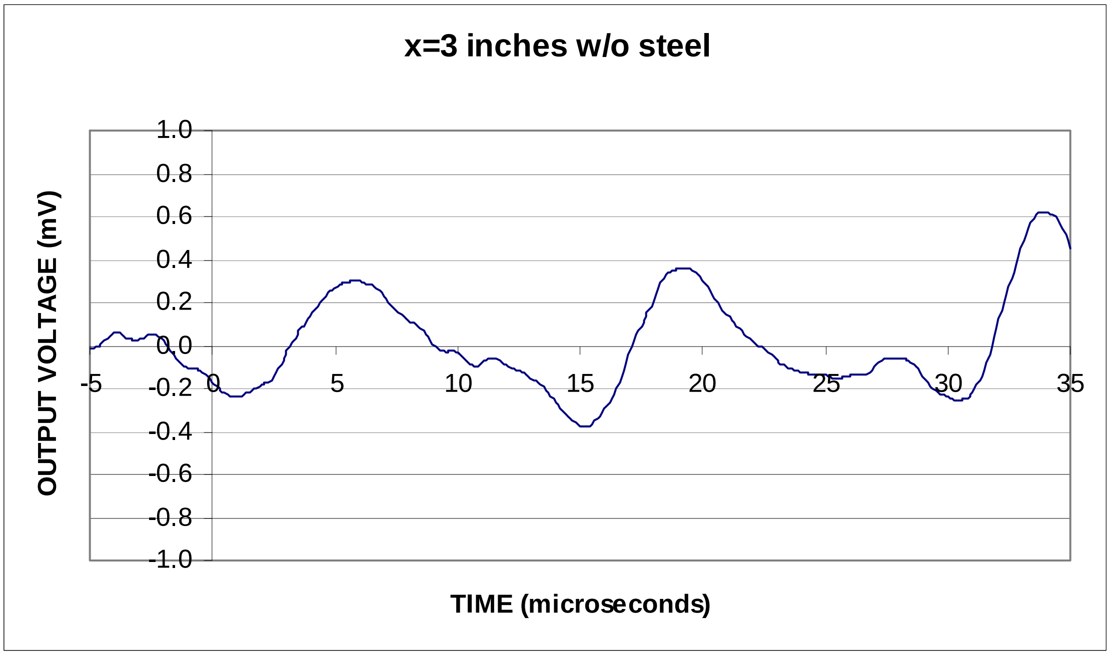

Figure A.4: Receiver sensor output in the un-reinforced concrete at position x=3 inches

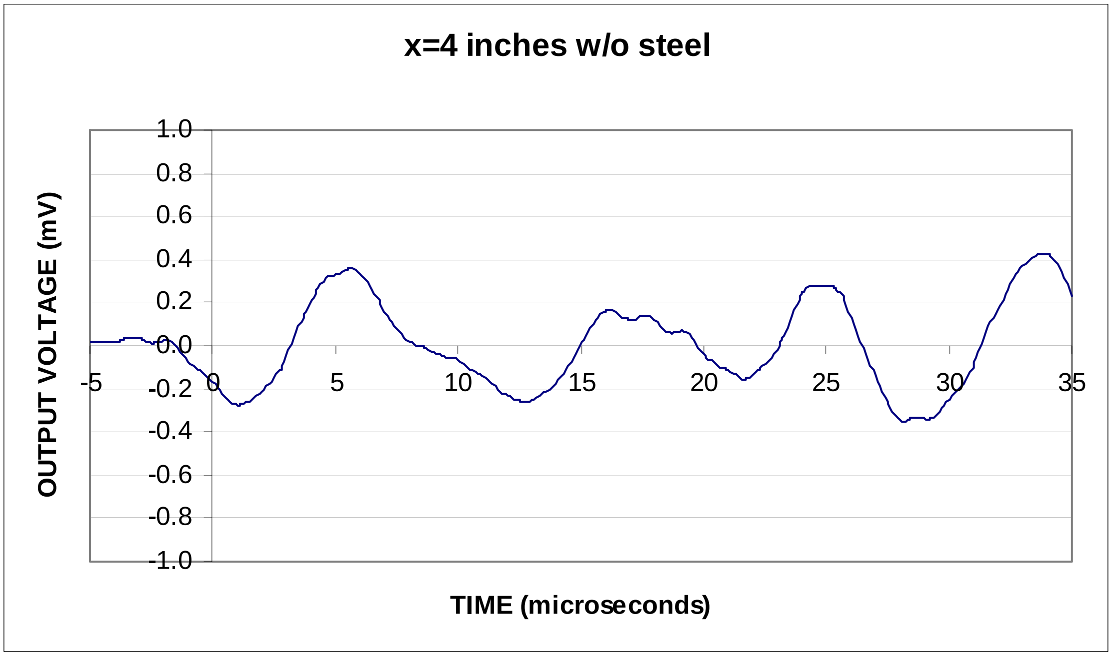

Figure A.5: Receiver sensor output in the un-reinforced concrete at position x=4 inches

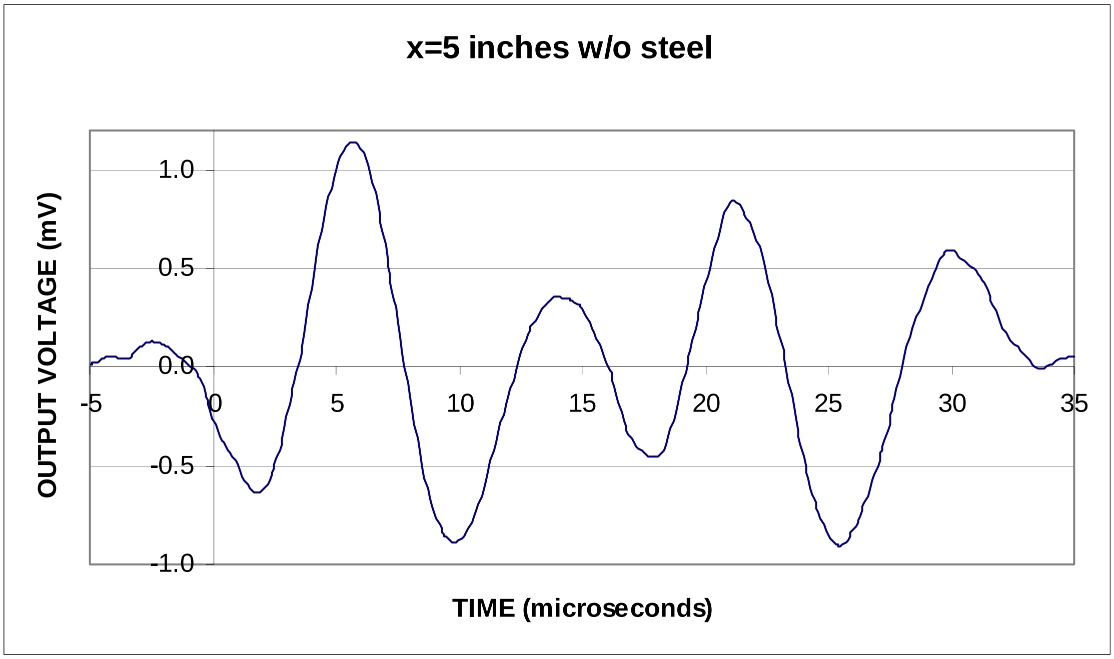

Figure A.6: Receiver sensor output in the un-reinforced concrete at position x=5 inches

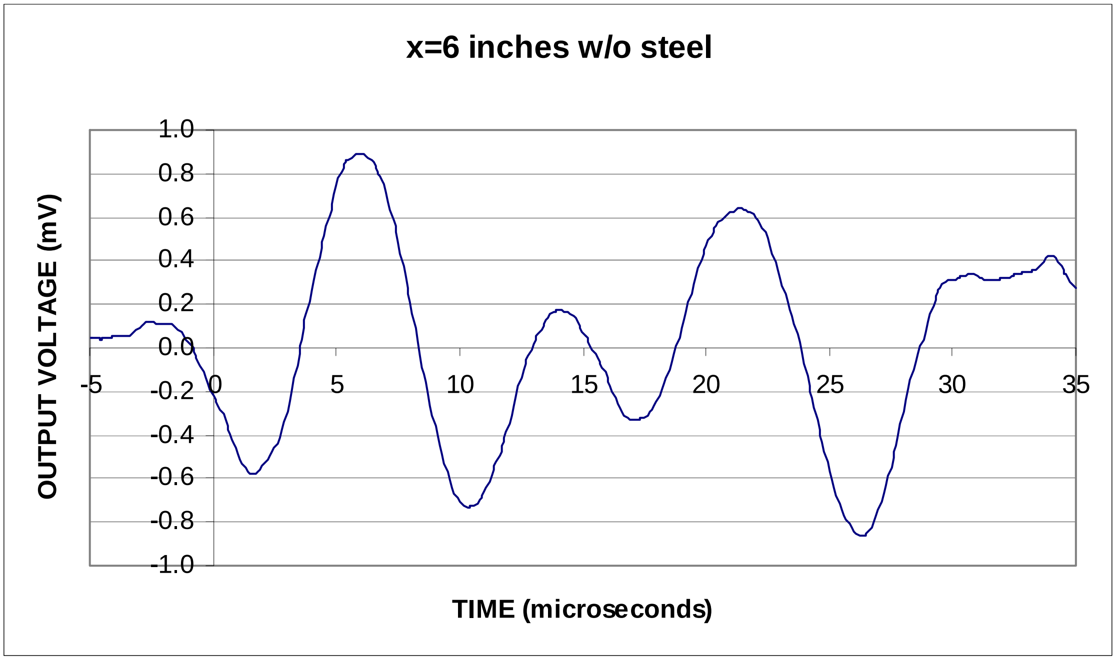

Figure A.7: Receiver sensor output in the un-reinforced concrete at position x=6 inches

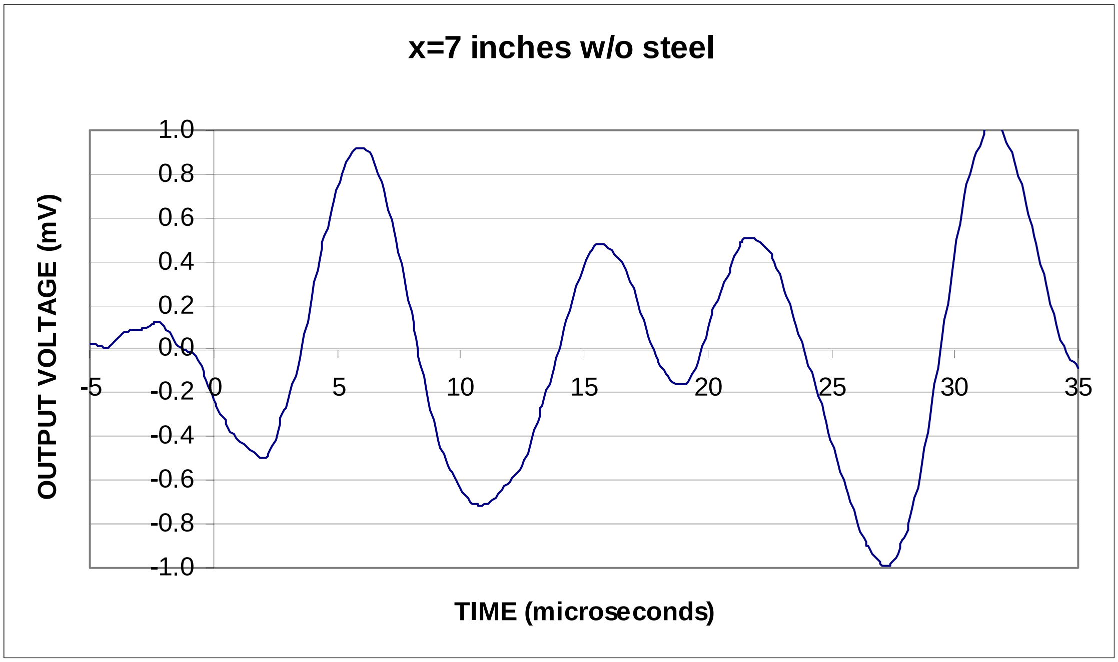

Figure A.8: Receiver sensor output in the un-reinforced concrete at position x=7 inches

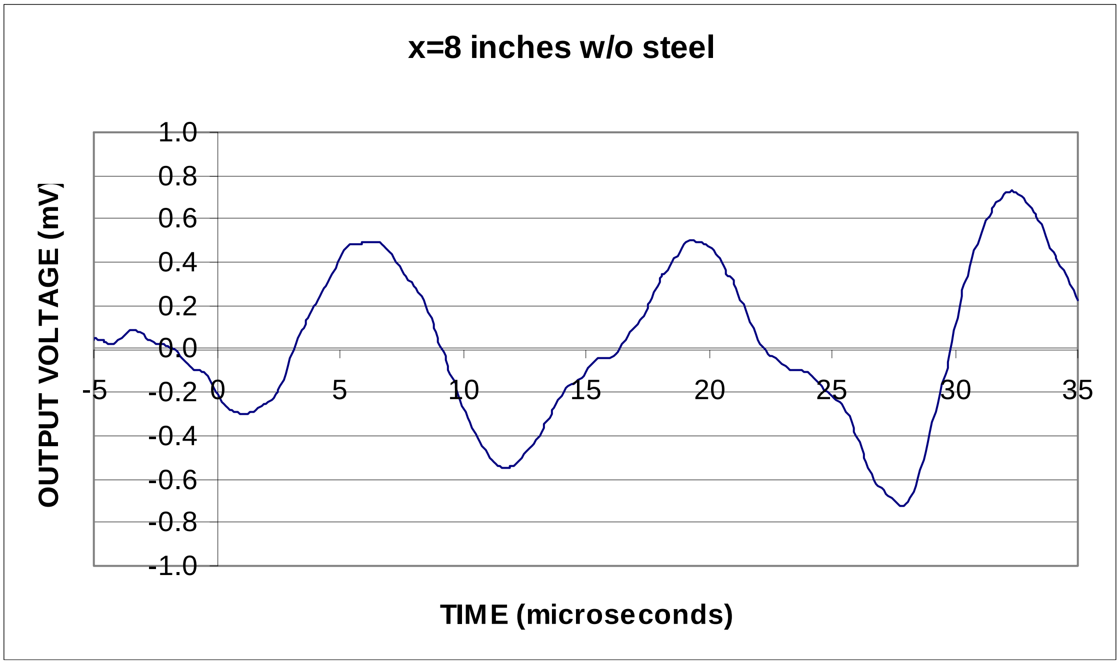

Figure A.9: Receiver sensor output in the un-reinforced concrete at position x=8 inches

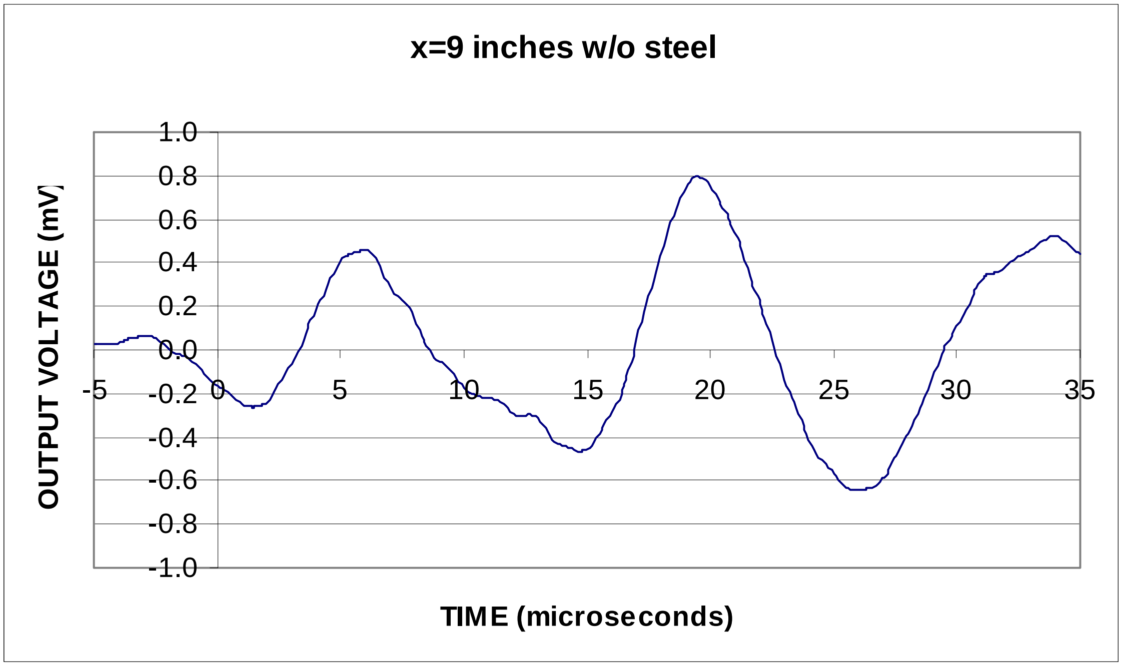

Figure A.10: Receiver sensor output in the un-reinforced concrete at position x=9 inches

APPENDIX B

The calculated vertical displacements described in section 4.1 are presented here.

Figure B.1: FEA results for the un-reinforced concrete block at position x=0 inches

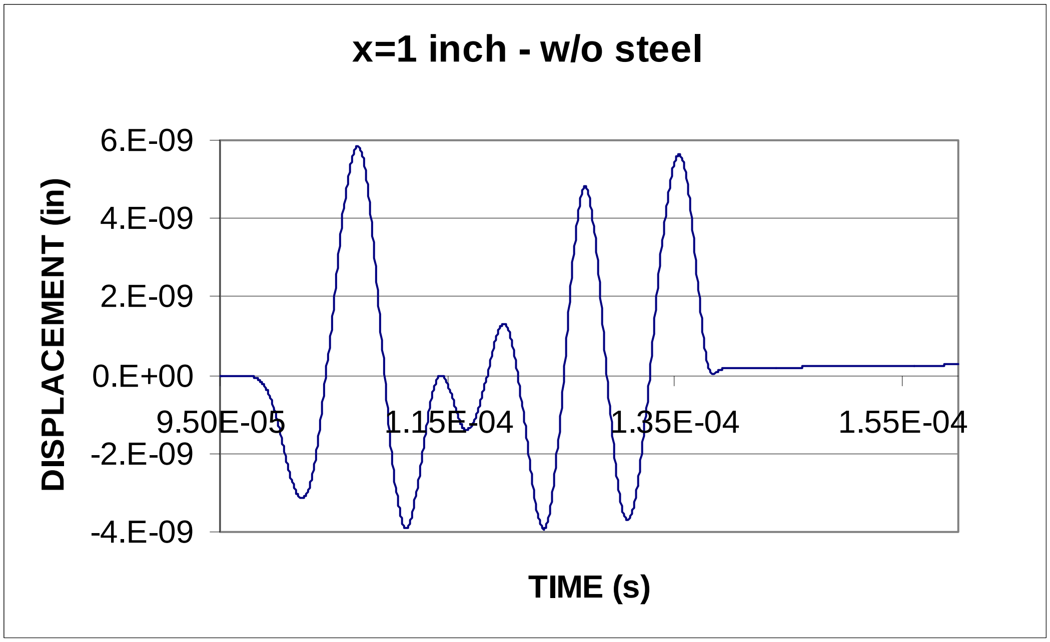

Figure B.2: FEA results for the un-reinforced concrete block at position x=1 inch

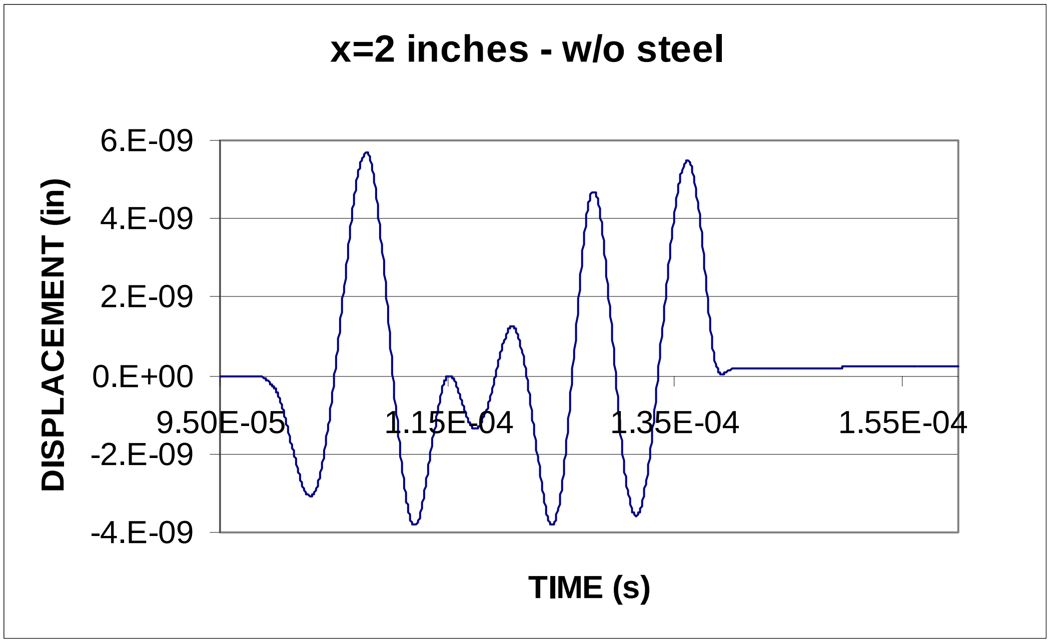

Figure B.3: FEA results for the un-reinforced concrete block at position x=2 inches

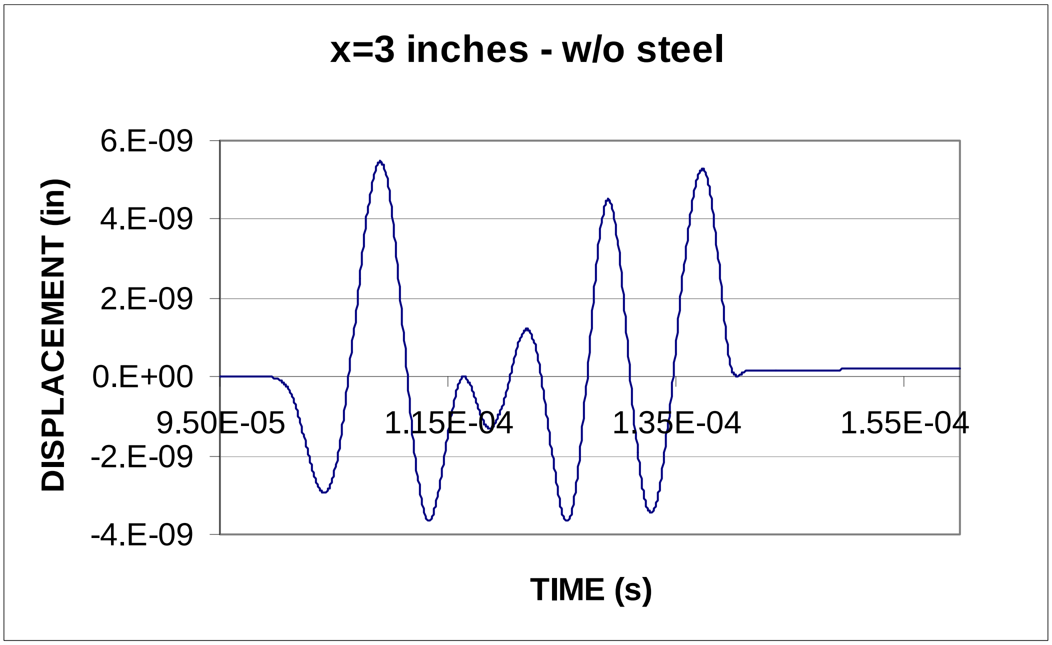

Figure B.4: FEA results for the un-reinforced concrete block at position x=3 inches

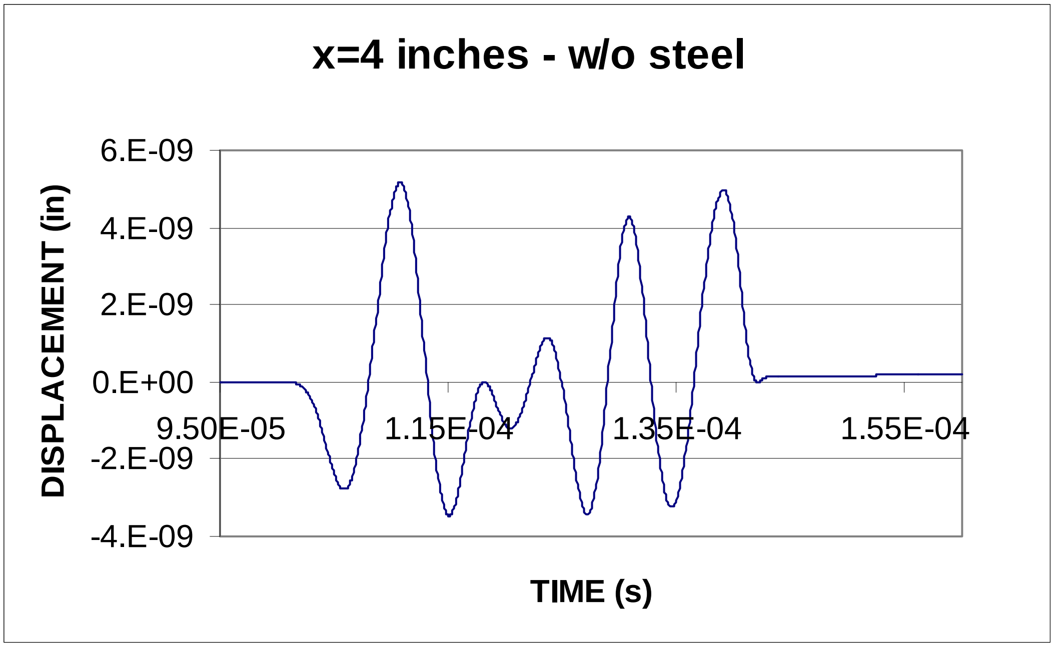

Figure B.5: FEA results for the un-reinforced concrete block at position x=4 inches

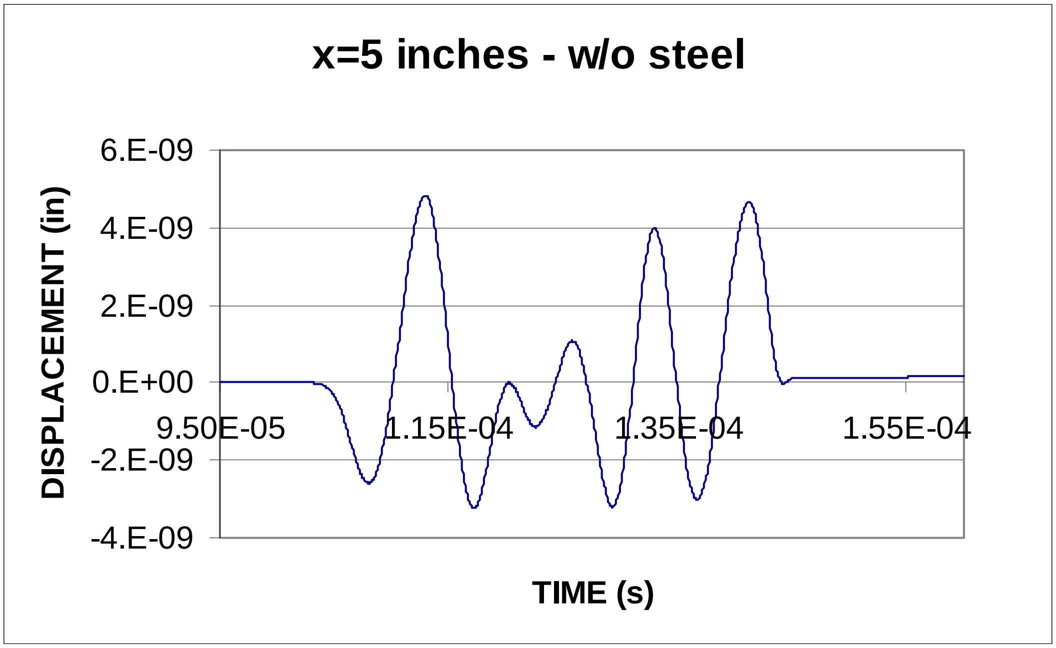

Figure B.6: FEA results for the un-reinforced concrete block at position x=5 inches

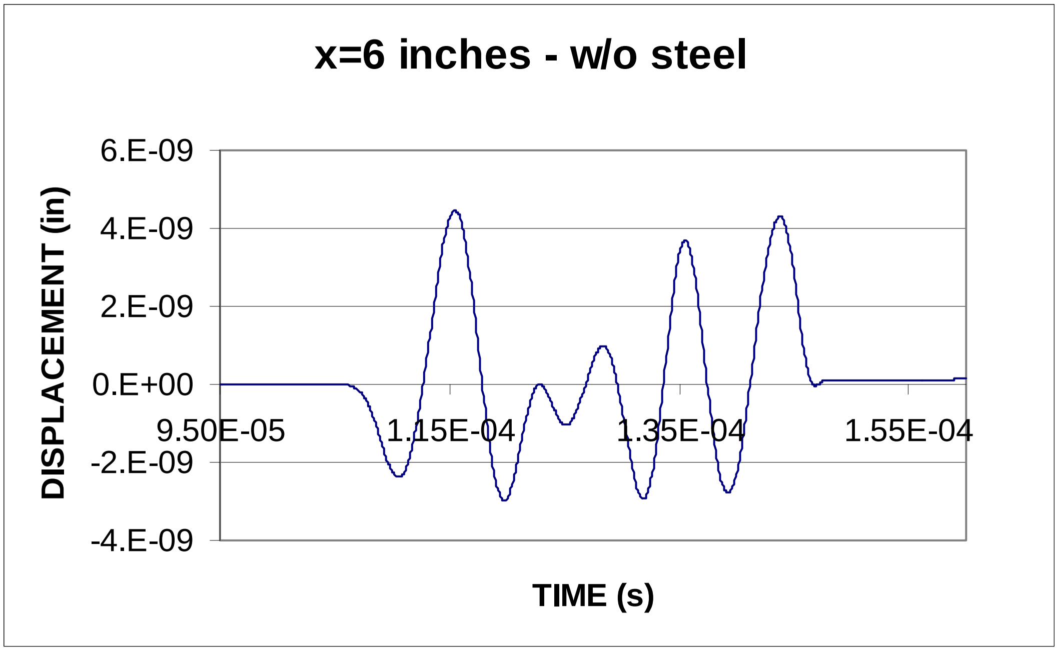

Figure B.7: FEA results for the un-reinforced concrete block at position x=6 inches

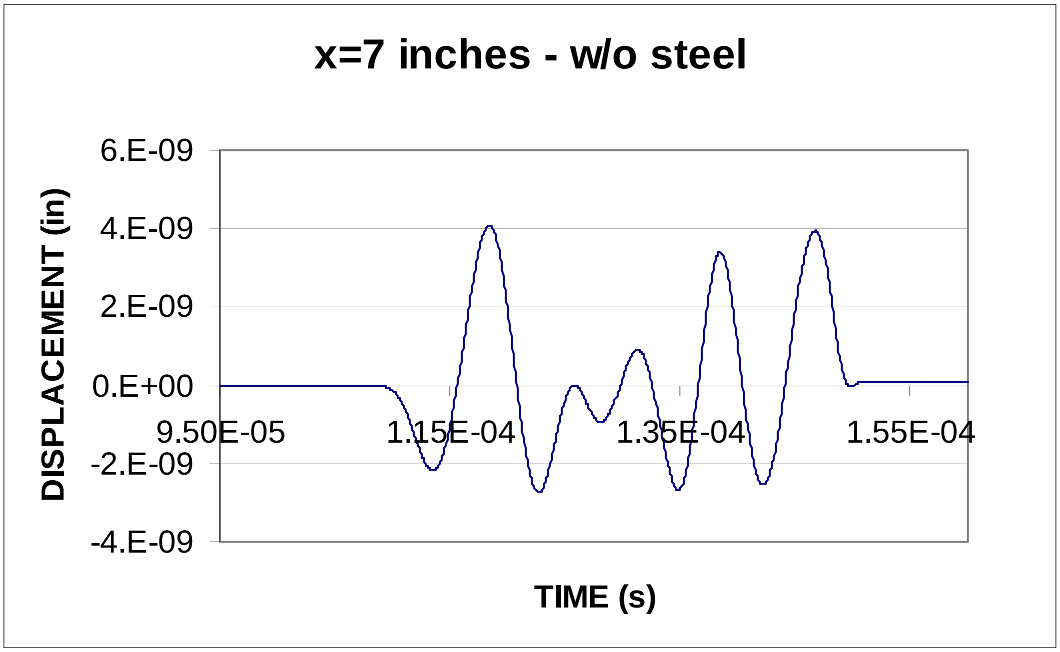

Figure B.8: FEA results for the un-reinforced concrete block at position x=7 inches

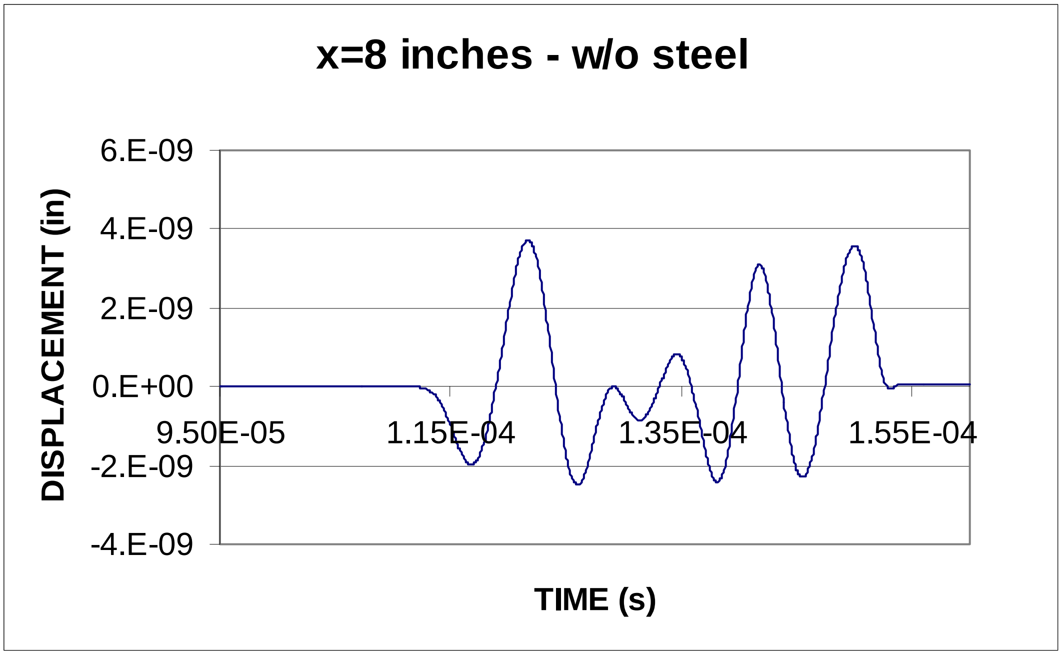

Figure B.9: FEA results for the un-reinforced concrete block at position x=8 inches

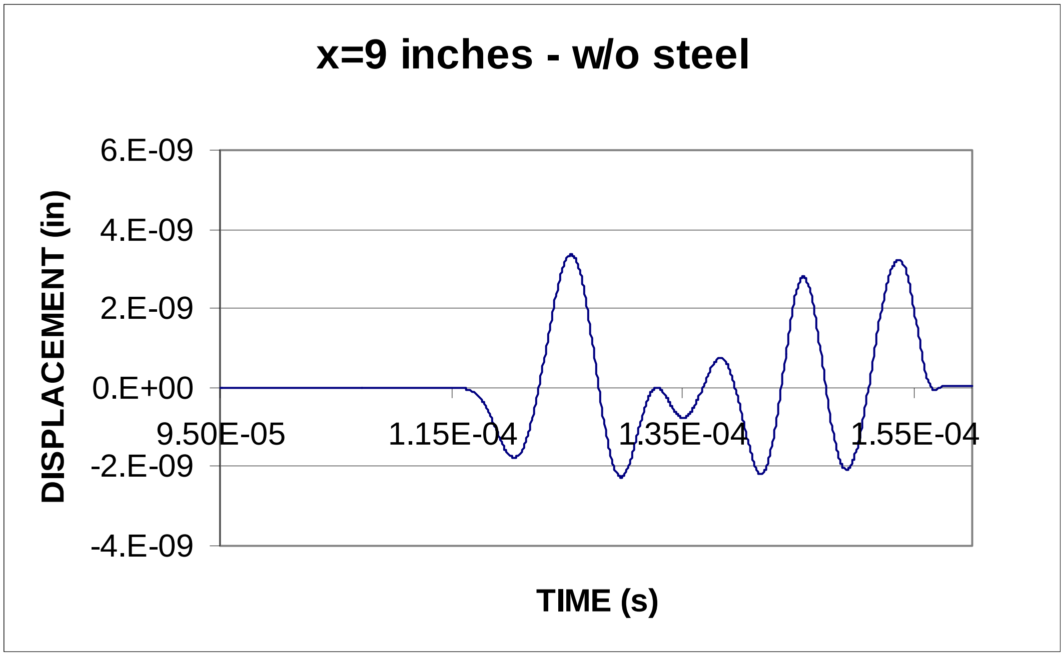

Figure B.10: FEA results for the un-reinforced concrete block at position x=9 inches

APPENDIX C

The sensor output from the tests described in section 4.2 is presented here.

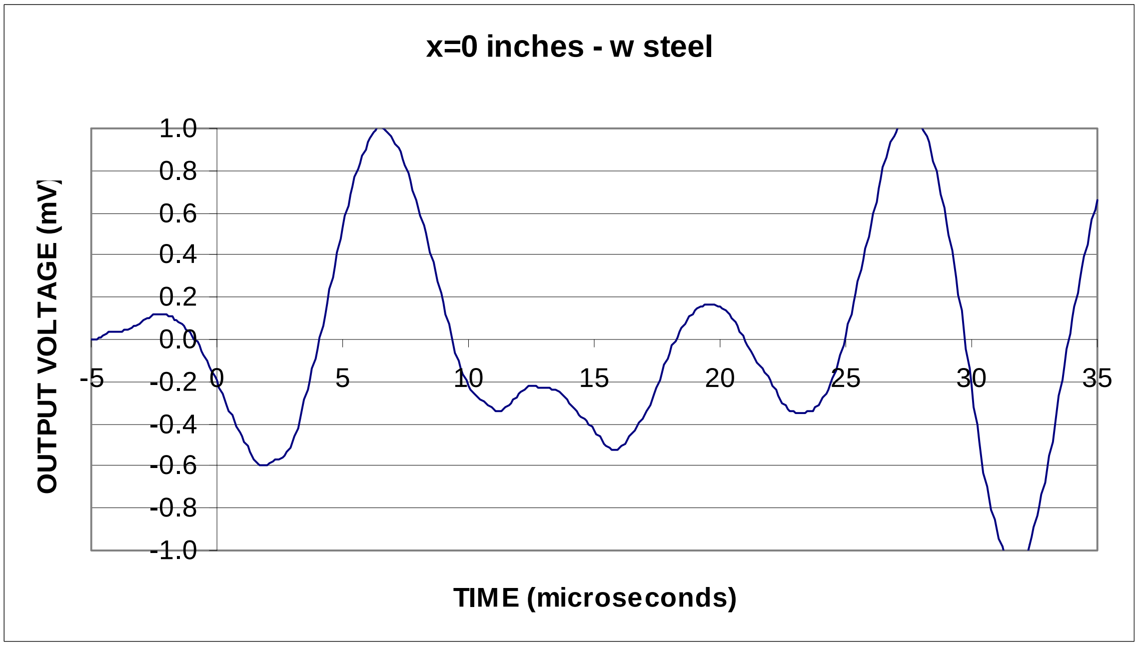

Figure C.1: Receiver sensor output in the reinforced concrete block at position x=0 inches

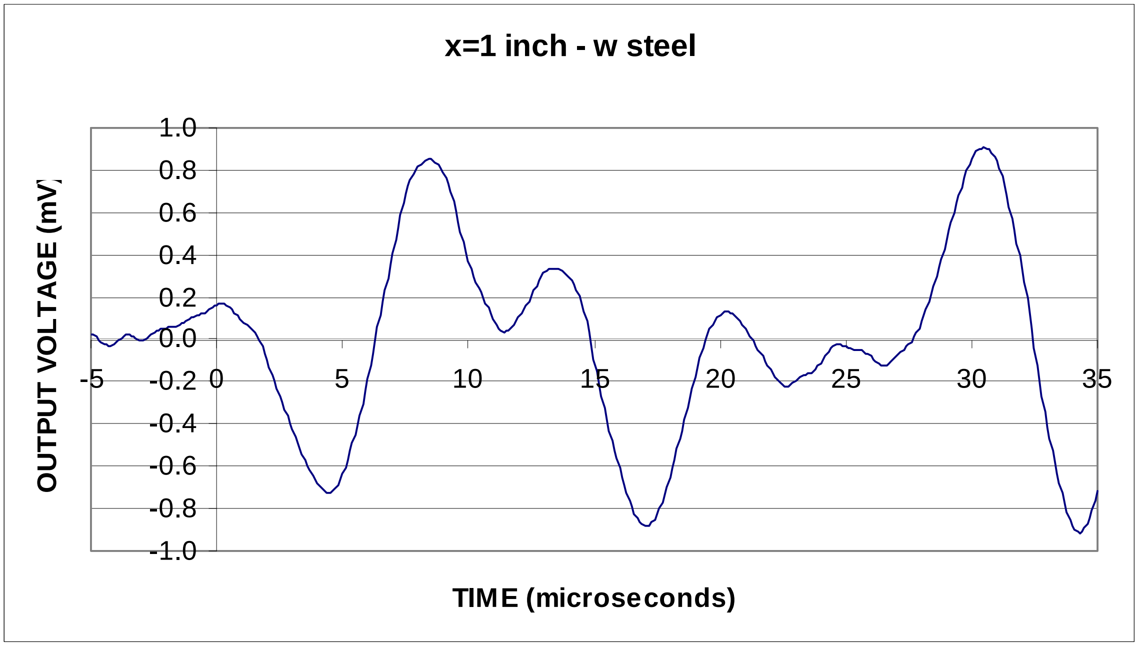

Figure C.2: Receiver sensor output in the reinforced concrete block at position x=1 inch

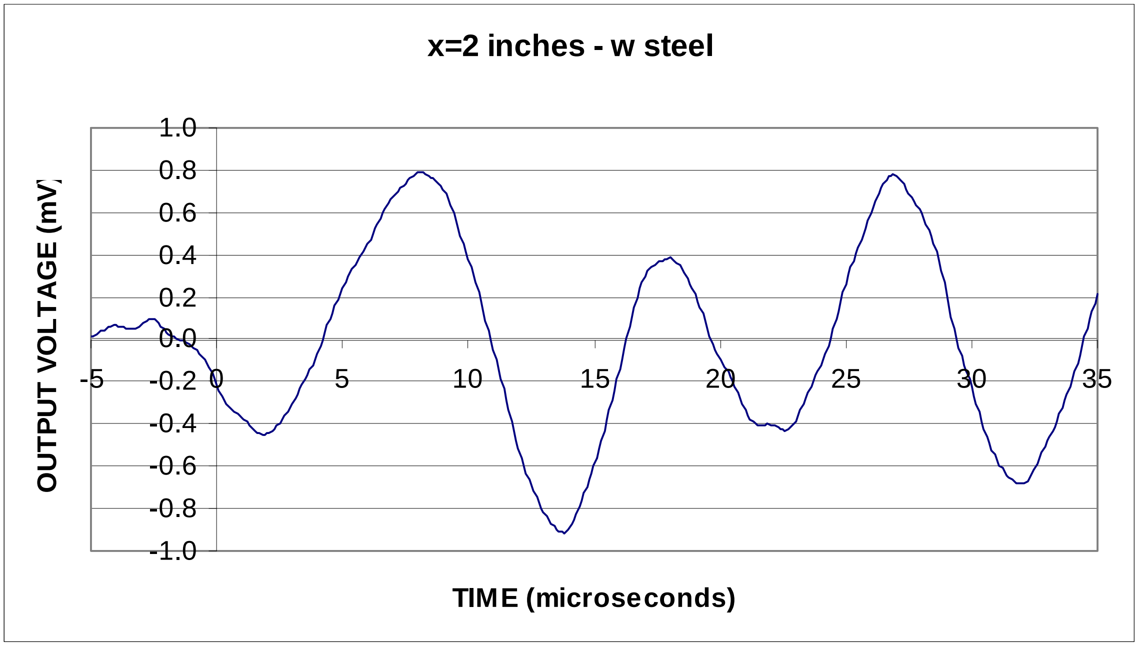

Figure C.3: Receiver sensor output in the reinforced concrete block at position x=2 inches

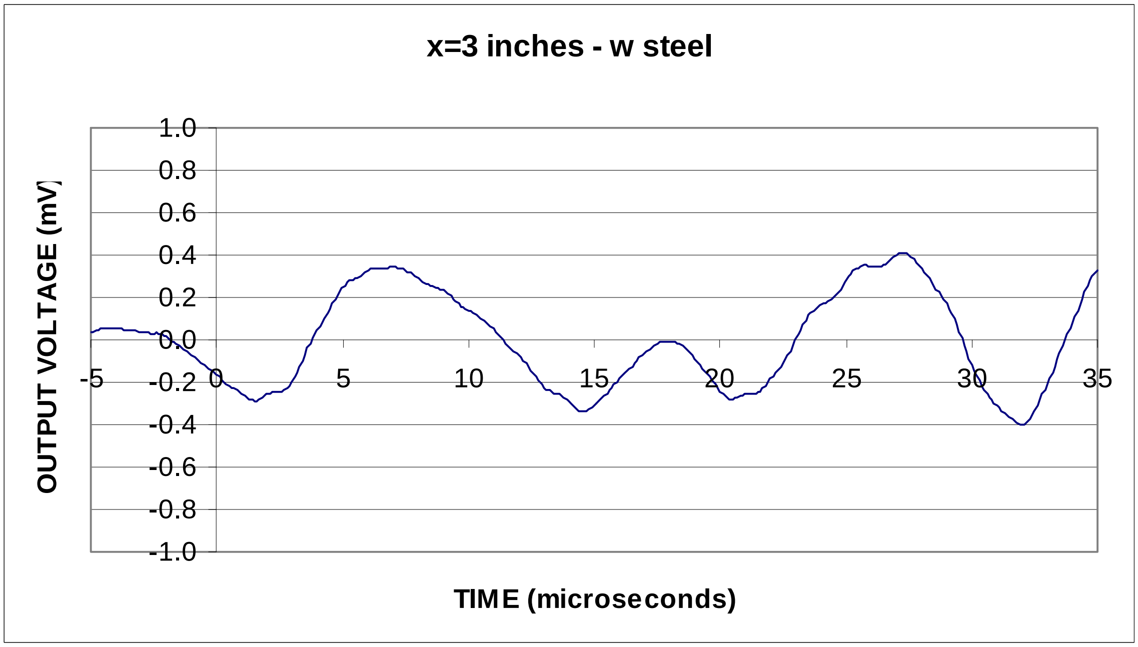

Figure C.4: Receiver sensor output in the reinforced concrete block at position x=3 inches

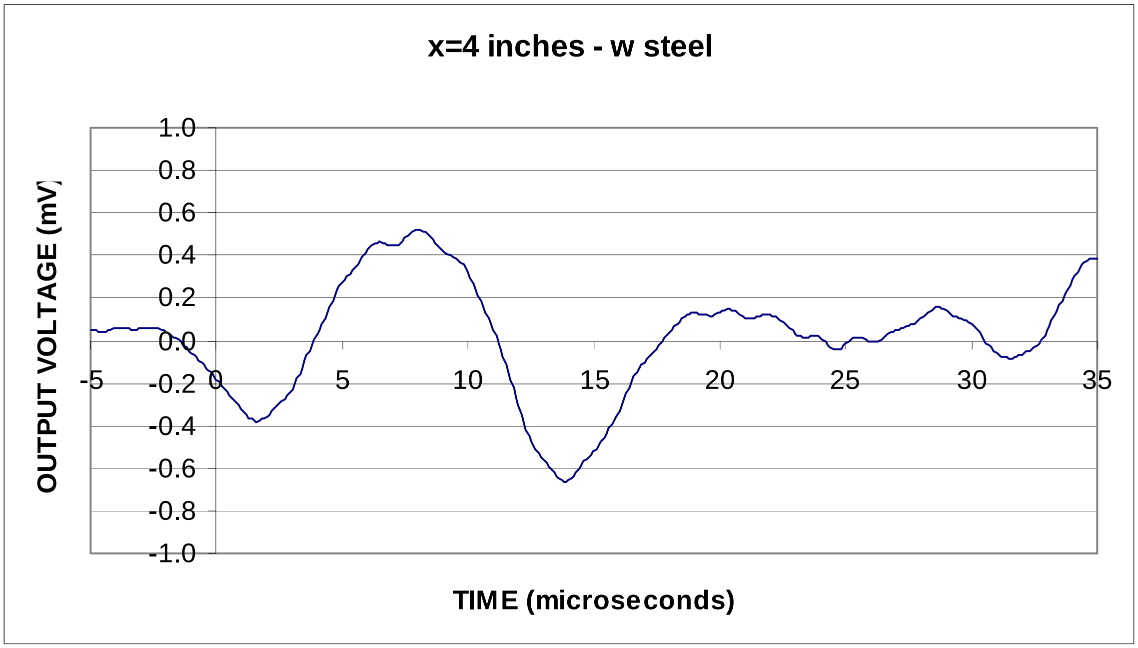

Figure C.5: Receiver sensor output in the reinforced concrete block at position x=4 inches

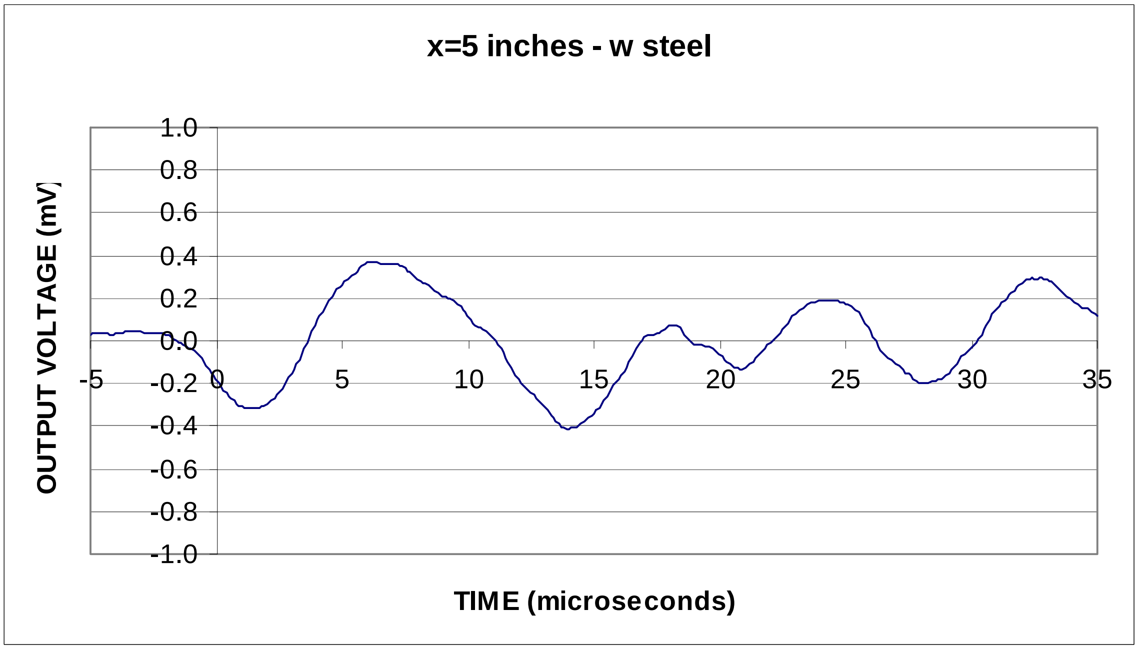

Figure C.6: Receiver sensor output in the reinforced concrete block at position x=5 inches

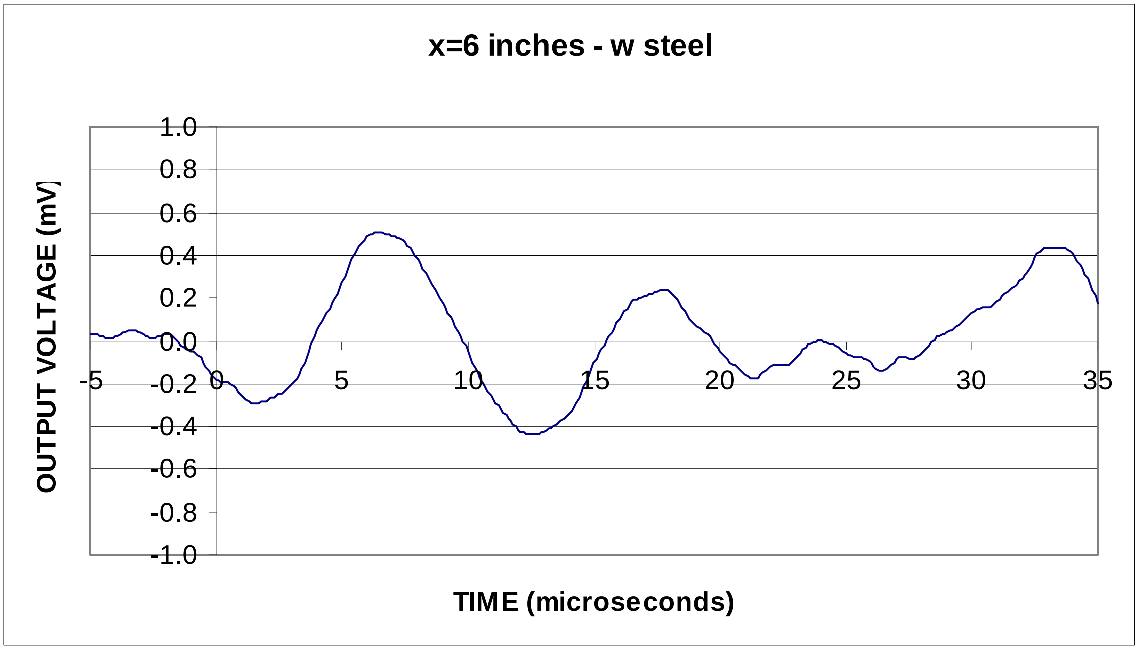

Figure C.7: Receiver sensor output in the reinforced concrete block at position x=6 inches

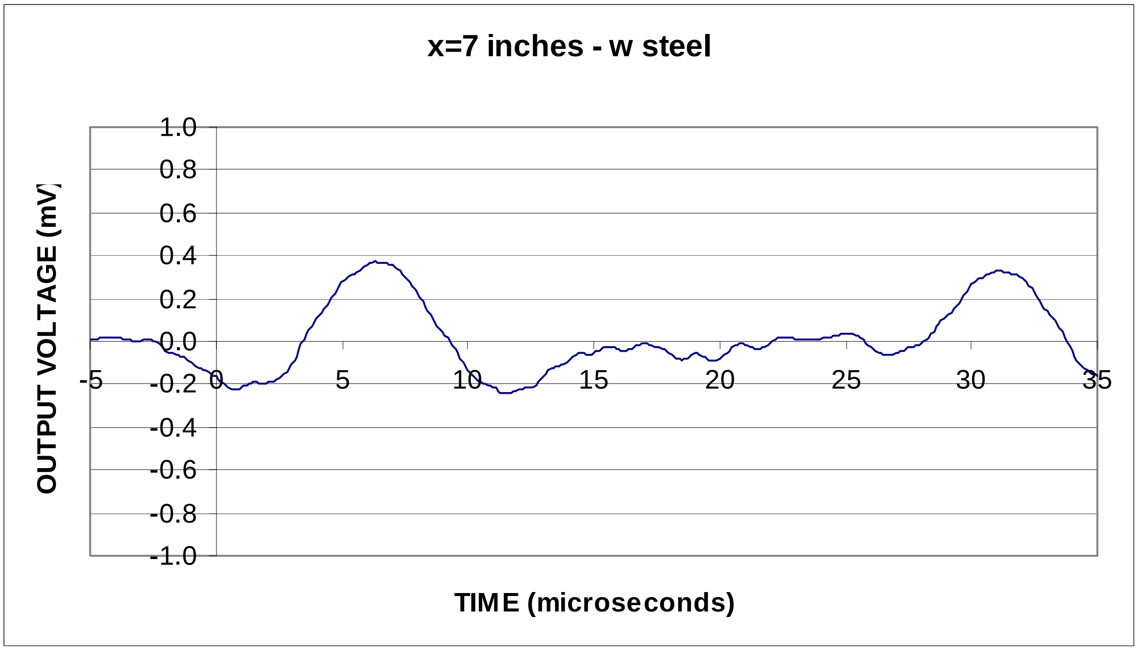

Figure C.8: Receiver sensor output in the reinforced concrete block at position x=7 inches

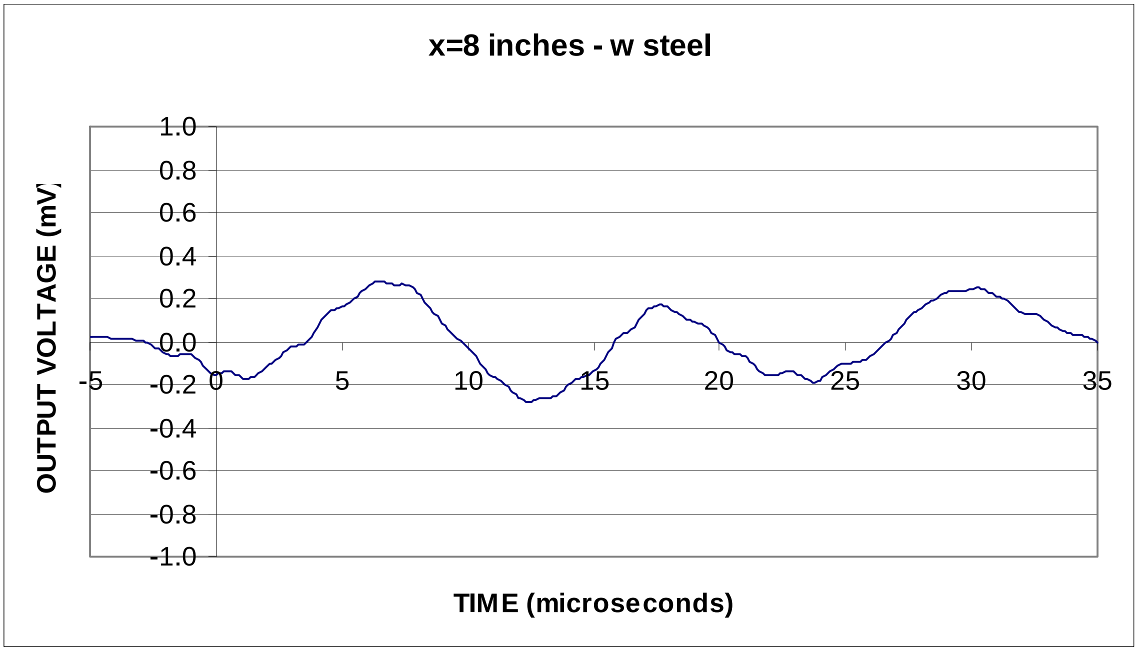

Figure C.9: Receiver sensor output in the reinforced concrete block at position x=8 inches

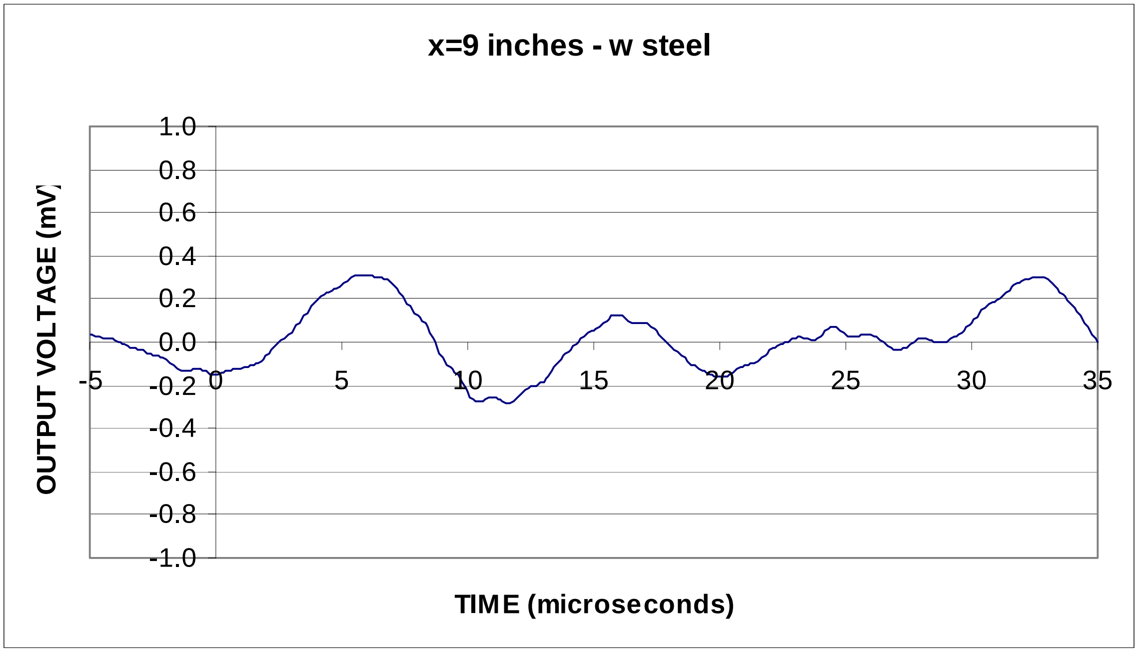

Figure C.10: Receiver sensor output in the reinforced concrete block at position x=9 inches

APPENDIX D

The calculated vertical displacements described in section 4.2 are presented here.

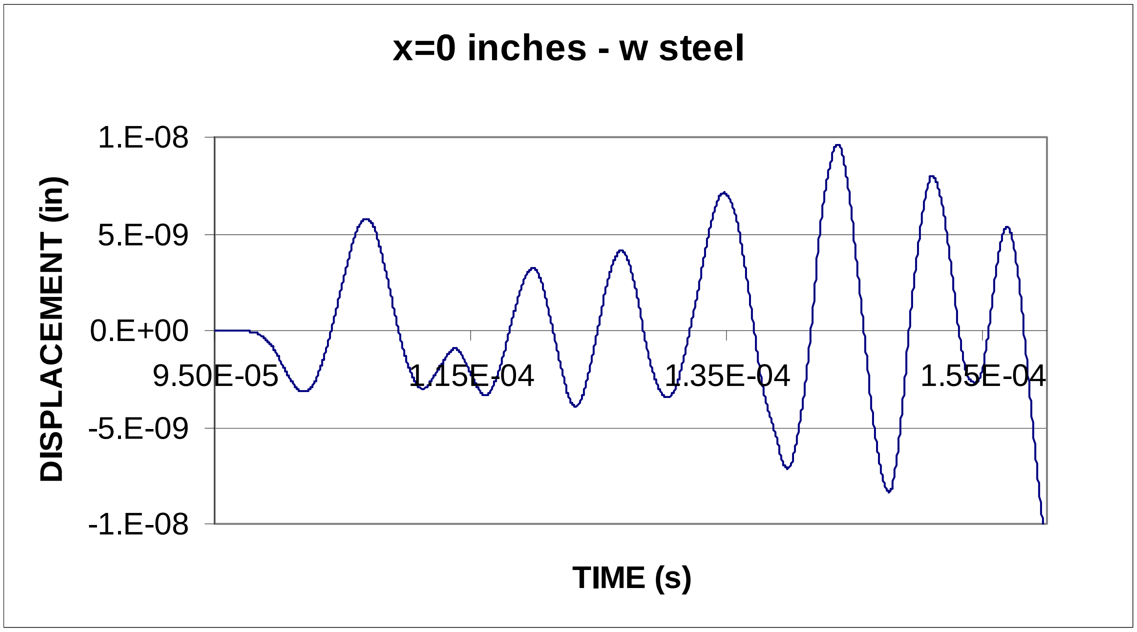

Figure D.1: FEA results for the reinforced concrete block at position x=0 inches

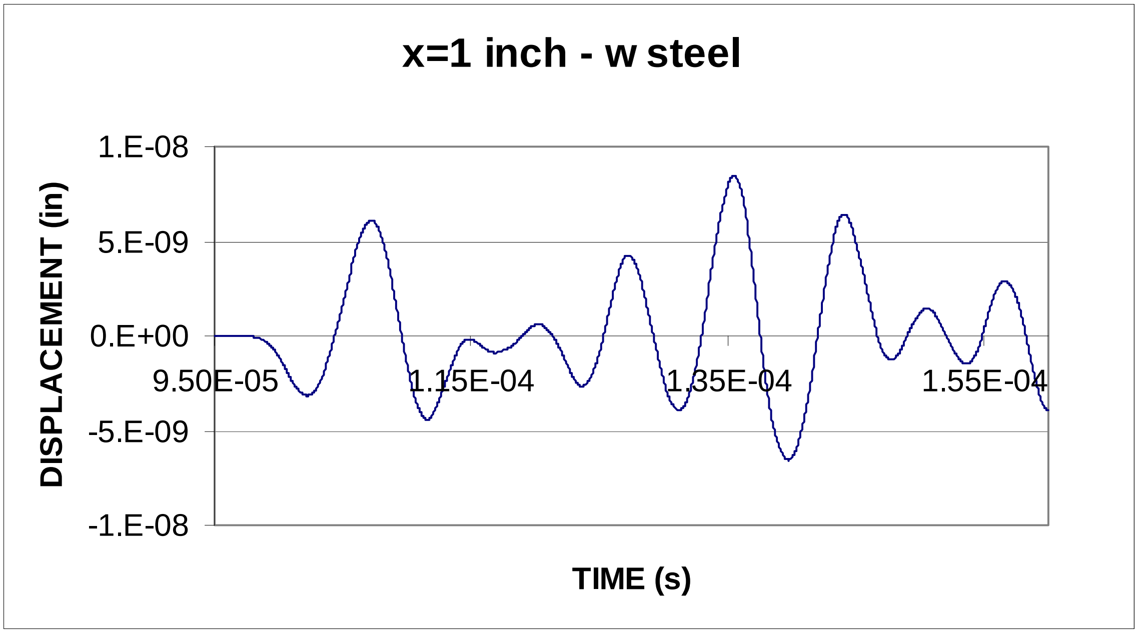

Figure D.2: FEA results for the reinforced concrete block at position x=1 inch

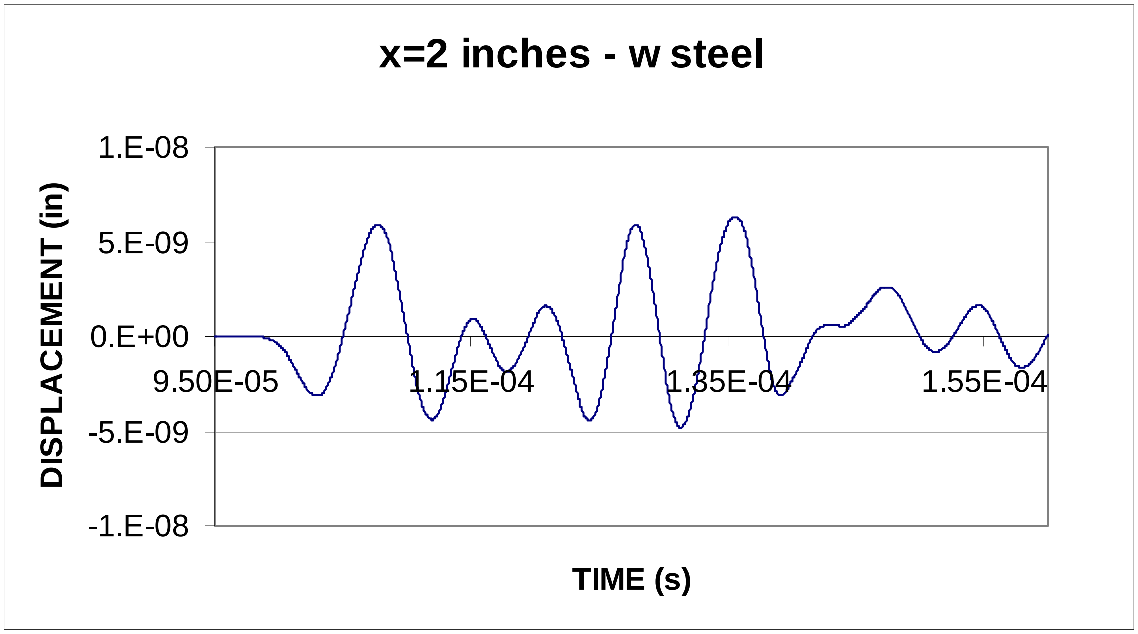

Figure D.3: FEA results for the reinforced concrete block at position x=2 inches

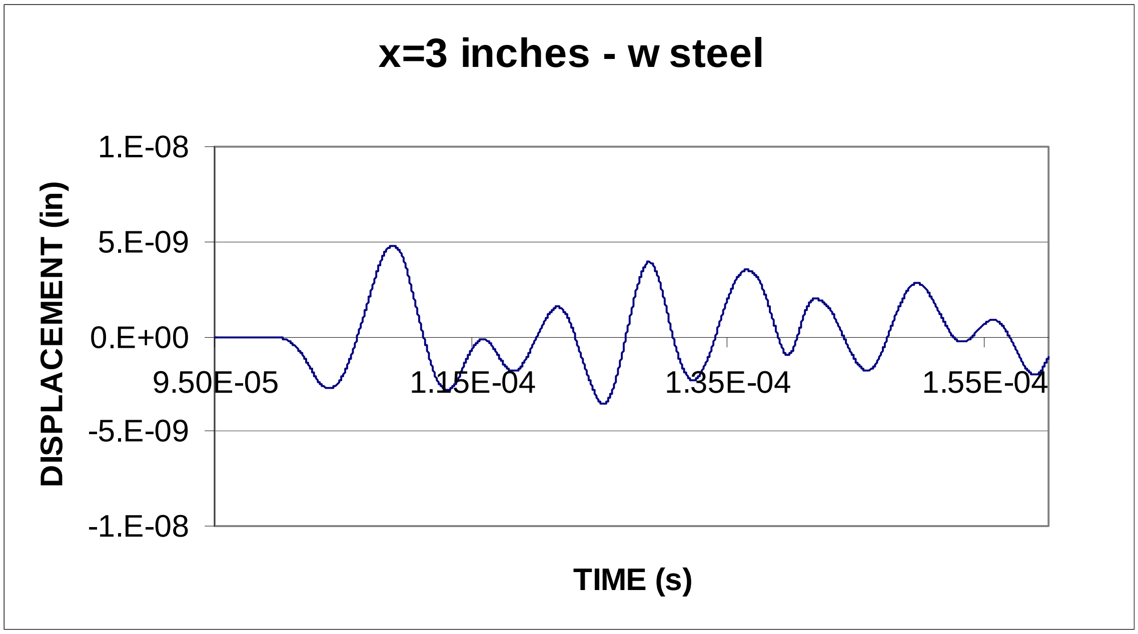

Figure D.4: FEA results for the reinforced concrete block at position x=3 inches

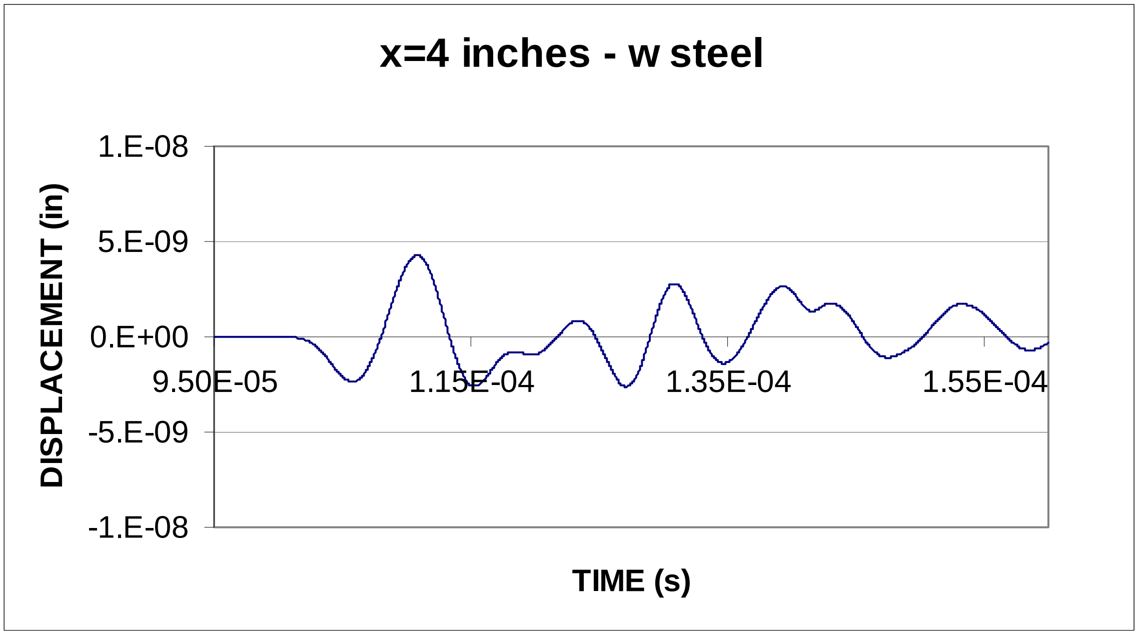

Figure D.5: FEA results for the reinforced concrete block at position x=4 inches

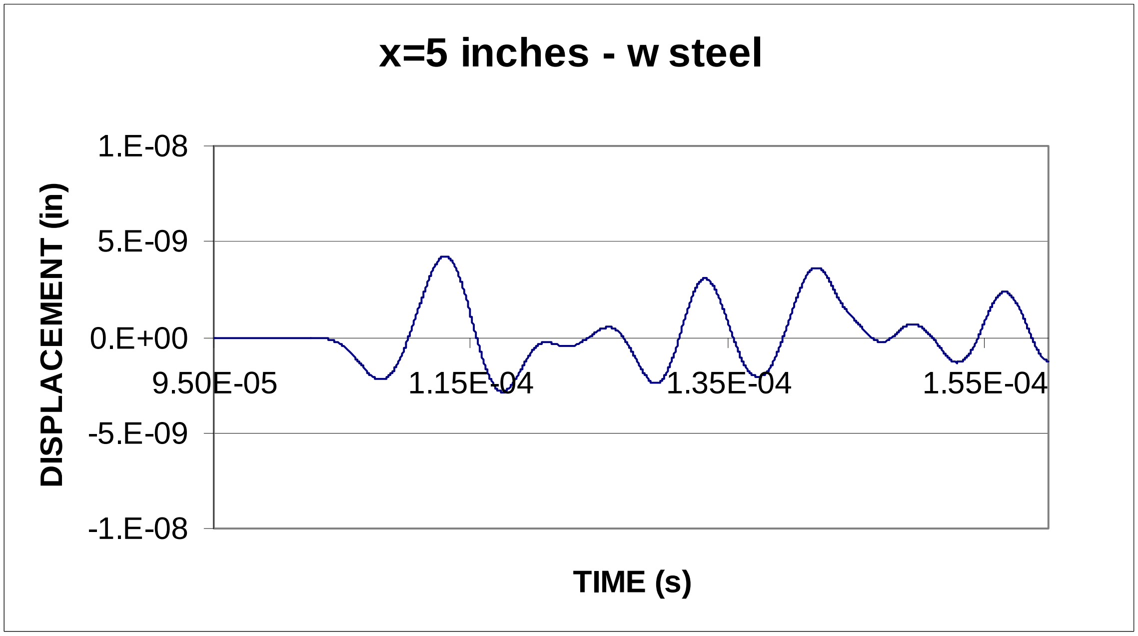

Figure D.6: FEA results for the reinforced concrete block at position x=5 inches

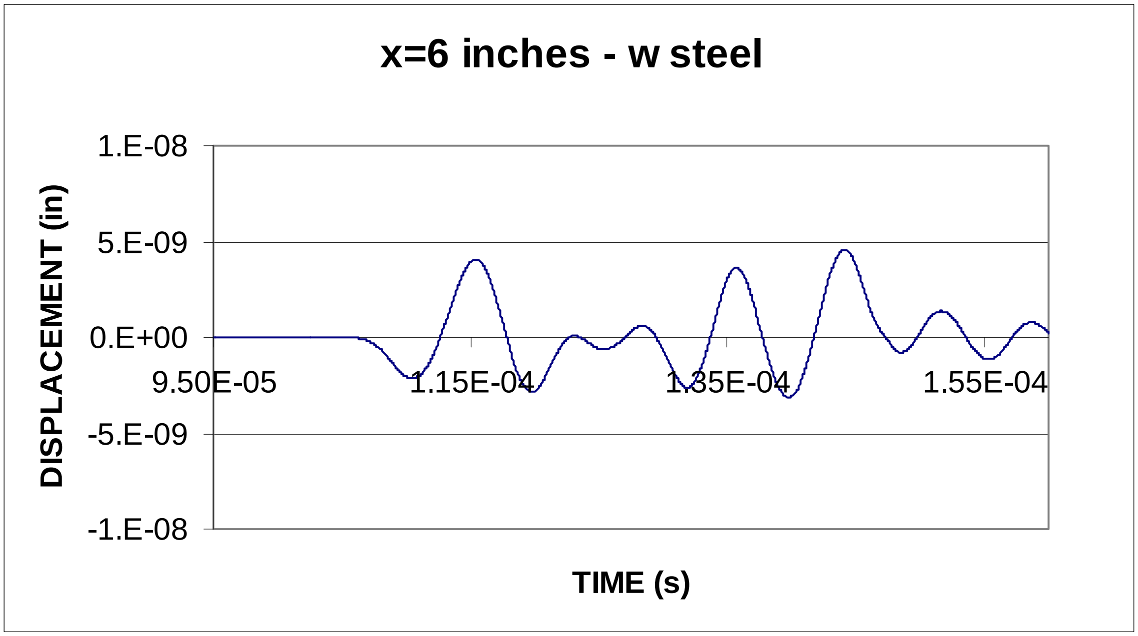

Figure D.7: FEA results for the reinforced concrete block at position x=6 inches

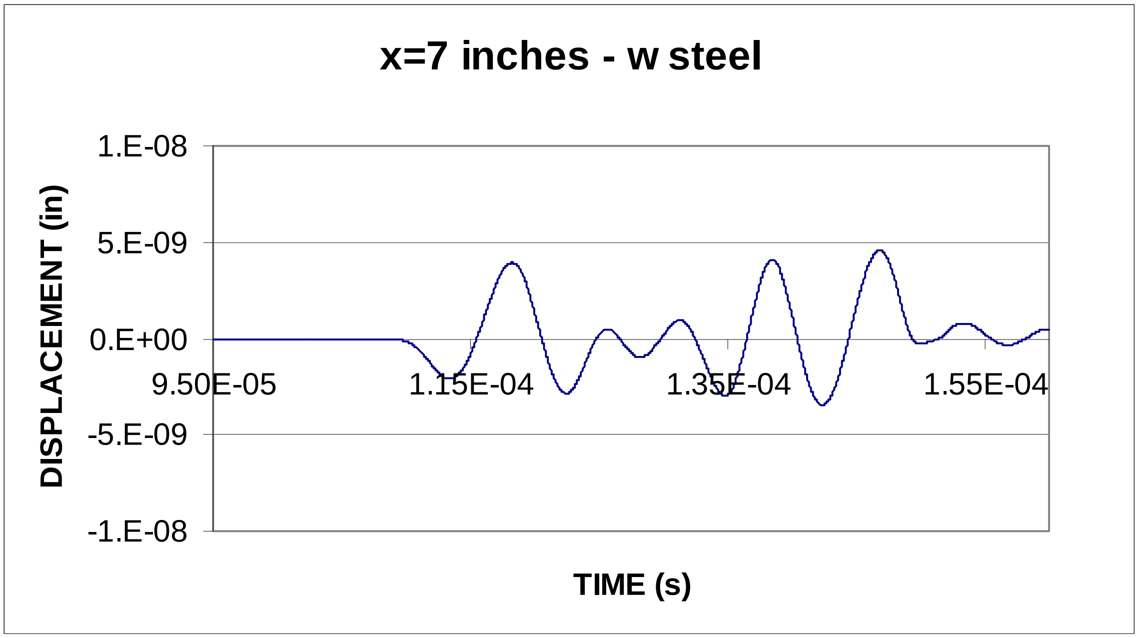

Figure D.8: FEA results for the reinforced concrete block at position x=7 inches

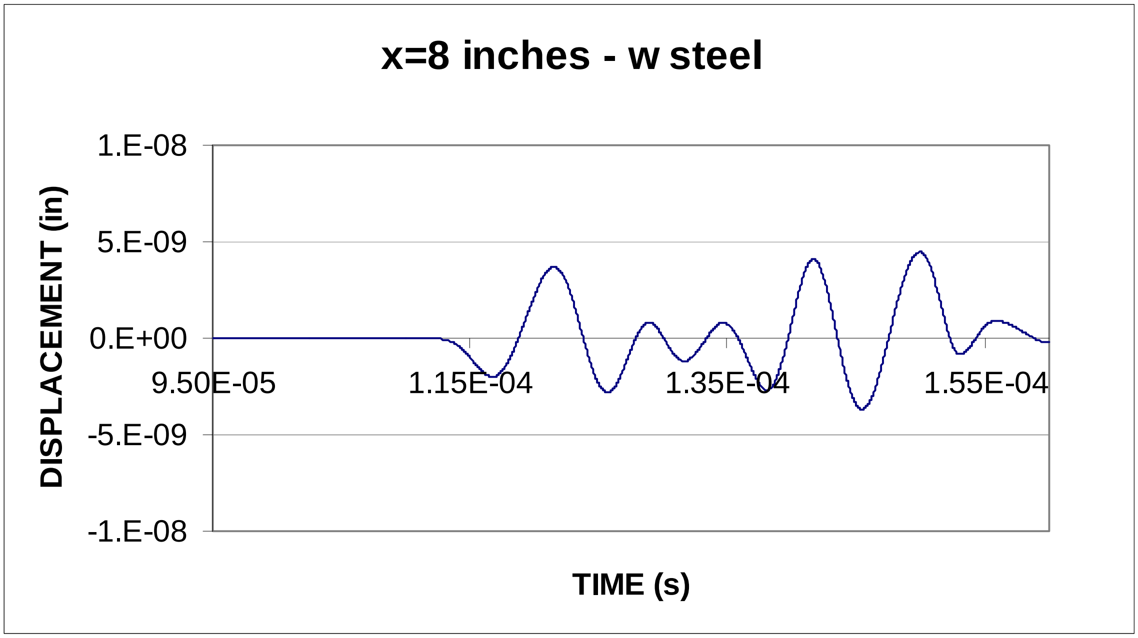

Figure D.9: FEA results for the reinforced concrete block at position x=8 inches

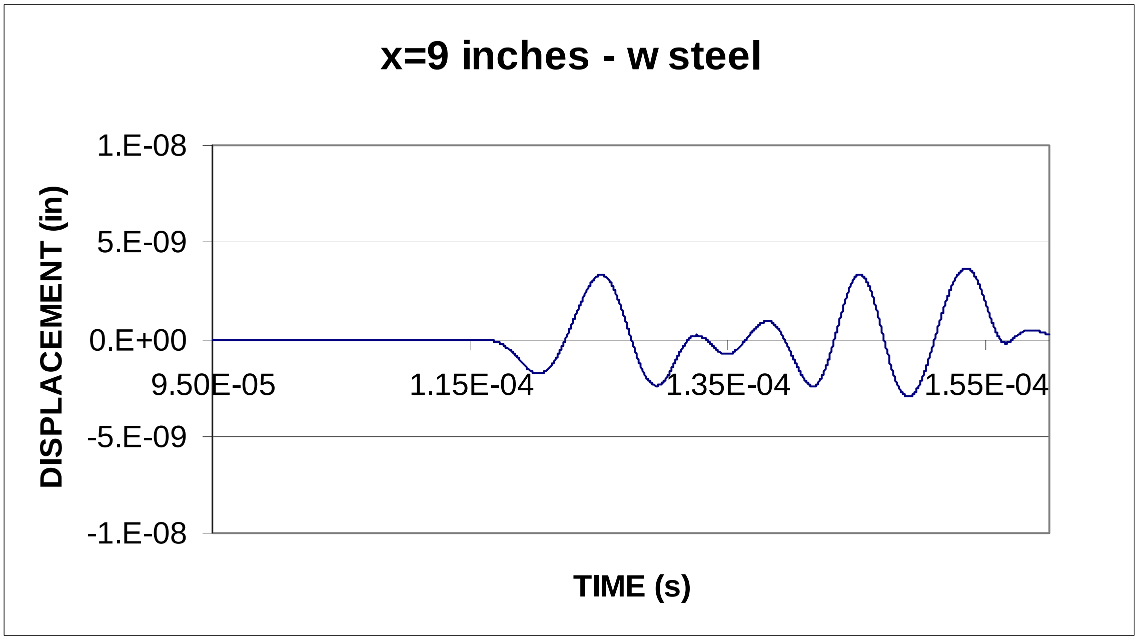

Figure D.10: FEA results for the reinforced concrete block at position x=9 inches

Three reports were produced from research sponsored by the Oregon Department of Transportation on acoustic emission (AE). "Acoustic Emission Techniques Applied to Conventionally Reinforced Concrete Bridge Girders" describes the evaluation of AE techniques applied to two reinforced concrete (RC) bridge girders, which were loaded to mimic in-service conditions. The main goal was to get a thorough understanding of how AE methods can be used with RC and in what way these methods can assist in maintaining the state's aging RC deck girder bridges. Recommended settings for data acquisition and processing were evaluated. In addition to the complex full-scale beam components, studies were performed on smaller test specimens that improved understanding of stress wave propagation through reinforced concrete and the response of acoustic emission sensors in detecting these waves. Some qualitative and quantitative assessment methodologies were described, and examples and limitations of the methods were presented. Source locations in three dimensions were performed, and strategies on how to best deploy sensors were evaluated using Monte Carlo Simulations. A method based on an analytical approach from seismology called *b*-value analysis was proposed to qualitatively estimate the maximum load level that a bridge has experienced. Some of the important findings and conclusions were:

- AE is the result of the change of a current structural condition state of a component.
- Main sources of AE from RC are crack formation and propagation.
- Changing boundary conditions (crack development) can influence AE parameters.
- Interpretation of AE data for a structure requires the critical values within the analysis methods to be customized for the structure. There are no standard threshold values for the analysis tools.
- AE appears to be well suited for long-term monitoring and real-time detection of structural degradation

Finite Element Modeling of Wave Propagation in Concrete details some basic research on modeling stress wave propagation in both not enforced and steel reinforced concrete using the finite element method. The FEM results agreed well with experimental results for the first oscillation of the stress wave, which is the part of the stress wave of most interest in many of AE analytical methods.

Acoustic Emission Testing of In-Service Conventionally Reinforced Concrete Deck Girder Superstructures on Highway Bridges presents practical guidelines for testing and evaluating bridges. The purpose of these guidelines is to allow the non-AE expert to design and implement a short term structural performance testing protocol or develop a long term structural health monitoring system.